J. Fluid Mech. (1993), *vol.* 257, *pp.* 691–721

Interactions between a free surface and a vortex sheet shed in the wake of a surface-piercing plate

By WU-TING TSAI AND DICK K. P. YUE

Department of Ocean Engineering, Massachusetts Institute of Technology, Cambridge, MA 02139, USA

(Received 22 February 1993 and in revised form 1 July 1993)

The nonlinear interactions between a free surface and a shed vortex shear layer in the inviscid wake of a vertical surface-piercing plate are studied numerically using a mixed-Eulerian-Lagrangian method. For a plate with initial submergence d starting abruptly from rest to constant horizontal velocity U, the problem is governed by a single parameter, the Froude number $Fn = U/(gd)^{\frac{1}{2}}$, where g is the gravitational acceleration. Depending on Fn, three classes of interaction dynamics (subcritical, transcritical and supercritical) are identified. For subcritical Fn ($\lesssim 0.7$), the free surface plunges on both the forward and lee sides of the plate before significant interactions with the vortex sheet occur. For transcritical and supercritical Fn, interactions between the free surface and the starting vortex result in a stretching of the vortex sheet which eventually rolls up into double-branched spirals as a result of Kelvin-Helmholtz instability. In the transcritical range ($Fn \sim 0.7$–1.0), the effect of the free surface on the double-branched spirals remains weak, while for supercritical Fn ($\gtrsim 1.0$), strong interactions lead to entrainment of the double-branched spiral into the free surface resulting in prominent surface features.

1. Introduction

The fundamental problem of the interaction between a free surface and a shear layer has attracted increasing attention in recent years motivated in part by the observation of persistent observable features in ship wakes. Considerable progress in both experimental investigation and numerical simulation of such phenomena has been made with emphasis on the interaction dynamics between the free surface and a given vortical flow. An example is the work of Yu & Tryggvason (1990), who study numerically the interaction of two-dimensional vortex flows with a free surface. The vorticity is modelled as point vortices, vortex sheets and vortex patches. They find that distinct free-surface motions are generated depending on the initial vortex configuration.

Another example is the numerical experiment of Dimas (1991) in which a shear flow with a mean velocity profile in the vertical direction is used to simulate the wake behind a two-dimensional submerged body. The Euler equations subject to free-surface boundary conditions are solved numerically. It is found that for a sufficiently large submergence, the interaction between the shear layer and the free surface is suppressed, and the flow reaches a quasi-steady state. For a smaller submergence, vortices form very near the free surface causing breaking surface

waves. The mechanisms involved in the interaction dynamics between the free surface and vorticity flow, however, were only partly identified. Moreover, no detailed quantification of the interaction features with respect to the submergence and velocity of the body was carried out.

The primary goal of this research is to identify and quantify, through careful numerical simulations, the basic mechanisms of the fully nonlinear body–vortex–free surface interactions including generation, evolution and the coupled dynamics. Of special interest is the understanding and quantification of the critical role of the Froude number.

To reach these objectives, we consider the canonical problem of a thin vertical surface-piercing plate of initial submergence d, moving abruptly from rest to a constant horizontal velocity U. The free surface rises sharply on the forward face and is drawn down on the rearward face into close proximity with the trailing vortex sheet shed from the lower edge of the strut. The resulting interaction dynamics among the body, free surface and the vortex sheet in the near-body wake are extremely complex and are not completely understood. Significantly, the present problem is governed by only a single parameter, the Froude number $Fn = U/(gd)^{\frac{1}{2}}$, where g is the gravitational acceleration, so that a systematic study varying this parameter allows us to reach a complete quantification and understanding of the underlying mechanisms.

One important distinction between this and previous computational studies is that the strengths and positions of the vorticity are not *prescribed* as initial conditions. The vortex shear layer here is shed by the strut under the influence of the free surface and vorticity flow, i.e. in the actual wake of the body. While the problem is simplified by a body possessing a sharp edge for which simple models for vortex generation can be used, the problem includes all the important interaction dynamics of vortex–body–free surface flows. Aside from fundamental scientific interests, the present problem may be of practical importance in the analysis of damping of shallow-draft bodies, the performance of lifting surfaces near a free surface, and the wave disturbances generated by the operation of such surfaces.

In the present work, the fluid is assumed to be inviscid and the free shear layer confined in an infinitesimal vortex sheet, outside of which the flow is irrotational. Thus the characteristics of a real, high-Reynolds-number flow are approximated by assuming the effects of viscosity to be confined to infinitesimally thin boundary and shear layers. The validity of such discrete-vortex approximations has been controversial, and has been the subject of vigorous debate since the pioneering work of Rosenhead (1931) and its subsequent criticism by Birkhoff & Fisher (1959). A comprehensive review of the various vortex methods and their practical applications can been found in Sarpkaya (1989), which also includes an extensive bibliography of these and related work.

For an infinitesimal vortex sheet, it is well known that the rate of growth of Kelvin–Helmholtz instabilities increases with the wavenumber of the disturbance (e.g. Lamb 1932) and the problem is strictly not well posed. In numerical simulations, such instabilities on a thin vortex sheet quickly manifest themselves and eventually destroy the calculation. In the physical problem, these absolute instabilities and singularities are absent due to the presence of viscosity. By introducing a small degree of numerical filtering (or damping) of the highest wavenumbers, the instability of the mathematical problem is likewise removed in the computational problem (Moore 1981; Krasny 1986*a*). It should be pointed out that such filtering or damping of short waves is essential in any inviscid model, since the presence of strong nonlinear interactions

will inevitably cause energy to transfer to and ultimately accumulate at the highest wavenumber modes represented.

Even when (a small amount of) filtering is applied, another instability has been shown to manifest itself after finite time (Moore 1979; Sulem *et al.* 1981; Meiron, Baker & Orszag 1982; Krasny 1986*a*) beyond which the curvature of vortex sheet becomes infinite at some point and the vorticity distribution forms a cusp. Although the existence of a solution to the mathematical problem after the appearance of the finite-time singularity is still unclear, the limiting numerical solution of the approximate equation such as in Krasny (1986*b*) indicates that the vortex sheet deforms into a double-branched spiral with an infinite number of turns centred at the singularity. In practice, if details of the local singular flow features are not of primary interest as in the present study, the asymptotically tightened and infinitely wound vortex roll-up singularity can be approximated by a single core vortex connected to a finite-winding-number vortex sheet (e.g. Pullin & Phillips 1981; Hoeijmakers & Vaatstra 1983) and the calculation of the outer vortex sheet roll-up can be continued.

Recently, using a desingularized equation (Chorin & Bernard 1973), Rottman & Stansby (1993) showed that the solution develops into a series of high-wavenumber double-branched spirals beyond the finite critical time. The precise cause of these fine structures is unknown and it is not certain whether they can be removed by filtering. In any event, it is unclear whether these are representative of possible features of the non-desingularized equation.

Like the simulation of an infinitesimal vortex sheet, numerical tracing of the free surface may also suffer instabilities (e.g. Longuet-Higgins & Cokelet 1976; see however Dold 1992). Thus the filtering/damping techniques for direct simulation of vortex and free-surface flows share many similarities. Some of the successful schemes include smoothing (Longuet-Higgins & Cokelet 1976 for a free surface; Moore 1981 for a vortex sheet), rediscretization (Fink & Soh 1978 for a vortex sheet; Dommermuth *et al.* 1988 for a free surface) and regularization methods (Chorin & Bernard 1973 for a vortex sheet). A common feature of all these techniques which stabilize the numerical scheme is the effective introduction of damping into the dynamical system, or of a filter which suppresses the unstable modes.

A common criticism of all these techniques is that the precise relationship between the computational results and the 'exact' mathematical solution and ultimately the actual physical problem is unclear. Our view is that with the limitations of the mathematical formulation in representing the physical model, and with the complexity of the physical system itself, there is much to be gained by accurate simulation and quantification of the global features despite the inevitable use of stabilizing techniques. The alternative of adopting full viscous free-surface simulations for high Reynolds numbers is otherwise prohibitive. We are especially encouraged by the promising results of Vinje & Brevig (1981) for simulation of nonlinear free-surface motions, and by Faltinsen & Pettersen (1982) for a vortex sheet shed from a moving body. Our goal is that, by performing accurate numerical simulations and systematic convergence tests especially with respect to the regularization parameters, a reliable description of the fundamental physical processes can be obtained.

Mathematical formulation of the mixed first- and second-kind Cauchy integral equations which describe the initial-boundary-value problem is given in §2. The mixed-Eulerian–Lagrangian method we employ and the detailed numerical implementation are described in §3. Of special importance is the use of cubic smoothing splines and an adaptive curvature-controlled rediscretization algorithm to suppress spurious short-wavelength instabilities and to optimize the resolution and efficiency

of the simulations. Extensive numerical tests to validate the accuracy and show the convergence of the numerical scheme are also presented. Detailed simulation results for the entire range of interest of the Froude number are given in §4. Three critical ranges of Froude number — subcritical, transcritical and supercritical — are identified based on the features of interaction between the free surface and the shed vortex sheet which are described in detail. Finally, physical properties of the motions which characterize the Froude-number dependence are presented. Preliminary results from this investigation were reported in a letter (Tsai & Yue 1991).

2. Mathematical formulation

2.1. *Mixed first- and second-kind integral equation*

We consider as a canonical problem the abrupt starting from rest to constant horizontal velocity U of an infinitesimally thin vertical surface-piercing strut of initial submergence d. A thin shear layer is shed from the edge of the submerged strut continuously as time proceeds. The flow, excluding the shear layer, is assumed to be inviscid, incompressible and irrotational which implies the existence of an analytic velocity potential $\phi(x, y, t)$ and stream function $\psi(x, y, t)$. We define Cartesian coordinates with the origin at the interaction point of the undisturbed free surface ($y = 0$) and the rest position of the plate ($x = 0$), with y positive upwards. For deep water, this problem is governed by only one parameter, the Froude number $Fn = U/(gd)^{\frac{1}{2}}$, where g is the gravitational acceleration. In the following, length and time units are chosen such that $d = g = 1$. The computational domain is enclosed by imposing periodic boundary conditions far up- and downstream (at $x = \pm\ell/2$). The contour of the solution domain consists of the free surface (C_f), the portion of the plate with fluid on one side (C_p), the submerged portion of the plate (C_s), and the vortex sheet (C_v).

Since the complex potential, $\beta(z, t) = \phi(x, y, t) + \mathrm{i}\psi(x, y, t)$, where $z = x + \mathrm{i}y$, is analytical inside the fluid domain, Cauchy's integral theorem gives for each time instant t

$$\beta(z_k, t) = \frac{1}{\mathrm{i}\pi} \int\!\!\!\!\!\!-_{C_f \cup C_p} \beta(z, t) K(z; z_k) \mathrm{d}z + \frac{1}{\mathrm{i}\pi} \int_{C_s \cup C_v} [\phi(z, t)] K(z; z_k) \mathrm{d}z + \mathrm{i}2\tilde{\beta}_\infty(t) \tag{2.1}$$

when $z_k \in C_f \cup C_p$, and

$$\beta^{\pm}(z_k, t) = \pm\tfrac{1}{2}[\phi(z_k, t)] + \frac{1}{\mathrm{i}2\pi} \int_{C_f \cup C_p} \beta(z, t) K(z; z_k) \mathrm{d}z + \frac{1}{\mathrm{i}2\pi} \int\!\!\!\!\!\!-_{C_s \cup C_v} [\phi(z, t)] K(z; z_k) \mathrm{d}z + \mathrm{i}\tilde{\beta}_\infty(t) \tag{2.2}$$

when $z_k \in C_s \cup C_v$. In the above, $[\phi(z, t)] = \phi^+ - \phi^-$ is the potential jump across C_s and C_v, and $\tilde{\beta}_\infty(t)$ is a complex constant resulting from contour integration along $z \in [-\ell/2 - \mathrm{i}\infty, \ell/2 - \mathrm{i}\infty]$. The kernel function,

$$K(z; z_k) = \left(\frac{\pi}{\ell}\right) \cot\left[\left(\frac{\pi}{\ell}\right)(z - z_k)\right], \tag{2.3}$$

is the complex potential which satisfies Laplace's equation inside the fluid domain excluding $z = z_k$ and a periodic boundary condition at $x = \pm\ell/2$.

We define the direction of contour integration in the anticlockwise sense such that the windward (leeward) side of the plate and shear layer are the positive (negative)

side of the contour. Taking the imaginary and real parts of (2.1) for $z_k \in C_f$ and C_p respectively, we obtain second-kind Fredholm integral equations for ψ on C_f and ϕ on C_p. The imaginary part of (2.2) when $z_k \in C_s$ gives first-kind integral equations for the potential jump $[\phi]$ on C_s. To avoid a weak singularity at the intersection point we specify the known β at both upper ($C_f \cap C_p$) and lower ($C_f \cap C_p \cap C_s$) intersection points (Lin 1984).

2.2. *Boundary and initial conditions*

On the plate surfaces C_p and both sides (+/−) of C_s, the prescribed uniform horizontal velocity gives the Neumann boundary condition in terms of the stream function:

$$\psi(x = t, y, t) = y \qquad (z \in C_p \cup C_s). \tag{2.4}$$

On the free surface C_f, the kinematic boundary condition is

$$\frac{\mathrm{D}z}{\mathrm{D}t} = \frac{\partial \beta^*}{\partial z} = w \qquad (z \in C_f), \tag{2.5}$$

where $\mathrm{D}/\mathrm{D}t$ is the material time derivative, and $w(z,t) = u(x,y,t) + \mathrm{i}v(x,y,t)$ is the complex velocity. From Bernoulli's equation, the dynamic boundary condition for zero atmospheric pressure on the free surface C_f gives

$$\frac{\mathrm{D}\phi}{\mathrm{D}t} = \tfrac{1}{2} w w^* - \frac{1}{Fn^2}\mathrm{Im}(z) \qquad (z \in C_f). \tag{2.6}$$

The vortex sheet C_v is a material surface with zero pressure jump across the shear layer and is convected according to

$$\frac{\mathrm{D}z}{\mathrm{D}t} = \tfrac{1}{2}(w^+ + w^-) \qquad (z \in C_v). \tag{2.7}$$

The unsteady Kutta condition at the separation point specifies that the flow leaves the trailing edge tangentially (i.e. vertically downwards). Such a condition ensures that at the trailing edge the velocity is finite and the pressure jump vanishes. Applying this Kutta condition to the unsteady Bernoulli's equation gives the rate of change of the shear layer strength leaving the tip of the plate:

$$\frac{\mathrm{D}[\phi]}{\mathrm{D}t} = \tfrac{1}{2}(w^- w^{-^*} - w^+ w^{+^*}) \qquad (z = t + \mathrm{i}). \tag{2.8}$$

The initial conditions at $t = 0$ are specified with the free surface quiescent ($\phi = 0$ and C_f : $\mathrm{Im}(z) = 0$) and a starting point vortex is shed using a similarity solution (e.g. Graham 1983) for its strength and position.

2.3. *Unsteady force and energy*

The unsteady horizontal force F_x acting on the plate can be calculated by integrating the pressure distributions on both sides of the plate. An alternative expression for F_x can be obtained from consideration of momentum conservation (e.g. Newman 1977), and is given for the present flow by

$$F_x = -\frac{\mathrm{d}}{\mathrm{d}t}\int_{C_f \cup C_p} \phi\, n_x \,\mathrm{d}s - \frac{d}{\mathrm{d}t}\int_{C_s \cup C_v} [\phi]\, n_x \,\mathrm{d}s - \frac{1}{Fn^2}\int_{C_f \cup C_p} y\, n_x^+ \,\mathrm{d}s, \tag{2.9}$$

where n_x is the horizontal component of the unit outward normal. The third integral vanishes in the present context of periodic conditions on the up- and downstream

boundaries. The first two integrals in (2.9) (due to the non-dimensionalization) also give the work done W on the fluid by the forced plate motion.

The total energy of the flow motions is

$$E = \frac{1}{2}\int_{C_f \cup C_p} \phi \, \mathrm{d}\psi + \frac{1}{2}\int_{C_s \cup C_v} [\phi] \, \mathrm{d}\psi + \frac{1}{2Fn^2}\int_{C_f} y^2 n_y \, \mathrm{d}s, \tag{2.10}$$

where n_y is the vertical component of the unit outward normal. The first and second integrals correspond to the kinetic energies of the free surface and vortex sheet motions respectively. The third integral represents the potential energy of the free surface. The inviscid flow formulation of the problem guarantees the conservation of energy, i.e. $W = E$.

3. Numerical implementation

3.1. *The mixed-Eulerian–Lagrangian method*

The initial-boundary-value problem (2.1)–(2.8) in §2, including the motions of the free surface, shear layer and moving plate, is solved using a mixed-Eulerian–Lagrangian approach. In order to solve the mixed first- and second-kind integral equations, contour integrations in (2.1) and (2.2) are approximated by representing the contour boundaries by piecewise-linear segments with piecewise-linear distributions of β and $[\phi]$ along the segments. The discrete forms of the mixed first- and second-kind integral equations are then solved by evaluating the integrations at suitable collocation points z_k. For the second-kind integral equations, the collocation points are on the nodes of the line segments. For the first-kind equations, the z_k are placed at the midpoints of the segments. In order to obtain two more equations for the complex constant $\tilde{\beta}_\infty(t)$, we also collocate at the upper intersection point and at the midpoint of the segment above the lower intersection point. Details of the numerical implementation in discretizing the integral equations can be found in Appendix A.

The evolutions of the free-surface position and potential are updated by integrating in time the kinematic and dynamic free-surface boundary conditions (2.5) and (2.6), using three-point Lagrange formulae for the complex velocity $w(z,t) = \partial\beta(z,t)/\partial z$. The velocities at the intersection points are obtained from differencing the nodal values of β on the plate below the intersection points. An explicit fourth-order Runge–Kutta scheme, which is conditionally stable for the linearized free-surface boundary conditions, is used to carry out the time integration.

The potential jump at the separation point of the plate is updated according to (2.8), where the velocities $w^{\pm}$ are calculated by differencing the values of $\beta^{\pm}$ at the midpoints of segments above the separation point using three-point Lagrange formulae. A new shear-layer segment is shed continuously at each time step. The new segment has an updated potential jump at the separation point, and the value of the shed potential jump from the previous time step at the other end which is convected from the separation point. The vortex shear layer is convected by a fourth-order Runge–Kutta integrating scheme according to the evolution equation (2.7).

3.2. *Adaptive rediscretization algorithm*

In order to control the growth of short-wavelength instabilities and to optimize the computational efficiency, we use a rediscretizing algorithm based on a cubic smoothing spline and a mesh-function-controlled node adjustment scheme. After the Lagrangian boundaries (C_f and C_v) are updated, smoothing cubic splines are calculated in the

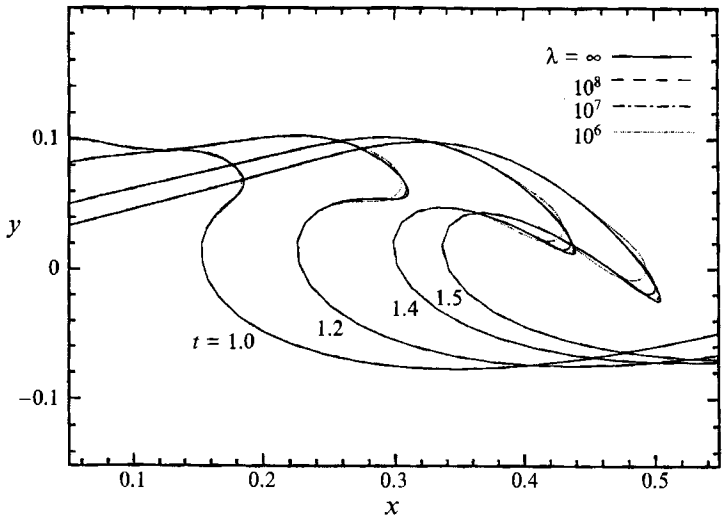

FIGURE 1. Free-surface profiles of a plunging breaking wave at $t = 1.0$, 1.2, 1.4 and 1.5 for different values of the smoothing parameter $\lambda = 10^6$, 10^7, 10^8 and ∞.

least square sense to fit the nodes of meshes (e.g. de Boor 1978; Lancaster & Šalkauskas 1990). The free surface and the shear layer are then rediscretized based on equidistribution of an appropriate mesh function (Hyman & Naughton 1985) on each segment. Details of the adaptive rediscretization algorithm are given in Appendix B.

Our computational experiments (Tsai 1991) show that the present adaptive rediscretization algorithm performs much more robustly and efficiently than the application of smoothing formulae (Longuet-Higgins & Cokelet 1976) or the use of equal-segment regridding for the mixed-Eulerian–Lagrangian method. As illustrations, we apply the adaptive rediscretization algorithm to two test problems which possess abrupt geometric changes and drastic evolutions: (i) a plunging free-surface wave; and (ii) the periodic double-branched spiral roll-up of a vortex sheet. The results are shown for systematic variations of the four parameters governing the rediscretization algorithm: the smoothing parameter λ, the mesh function increment I_κ, and the maximum and minimum segment sizes $h_{\max}$ and $h_{\min}$.

We generate a plunging breaking wave by imposing, as an initial condition, a sinusoidal free-surface profile of unit wavelength and 0.1 steepness and a surface potential corresponding to a *linearized* Airy wave. This wave develops in time under the effect of gravity and eventually turns over in a plunging wave. We follow this development with 80 Lagrangian points per wavelength without nodal redistribution but apply a smoothing spline fitting to the free-surface nodal positions and potentials every fifth time step.

Figure 1 shows the evolution of the free-surface profiles for different values of the smoothing parameter: $\lambda = 10^6, 10^7, 10^8$ and ∞. The infinite λ corresponds to the absence of any smoothing effect. The free-surface profiles are indistinguishable for the range of λ used except near the tips of the plunger. Near the tip, the profiles quickly converge to the non-smoothed one with increasing λ. The absolute error in the volume conservation and the percentage total energy loss for the different λ values are summarized in table 1. The volume error is less 10^{-4} and the energy loss is less than 1% of the total energy up to the re-entry of the plunger near $t = 1.5$.

The effect of changing the maximal segment size $h_{\max}$ and the mesh function

	Volume error			Energy loss (%)		
λ	$t = 1.2$	1.4	1.5	$t = 1.2$	1.4	1.5
10^6	0.000383	0.000480	0.000510	0.3395	0.6793	0.9415
10^7	0.000343	0.000407	0.000414	0.4101	0.8005	1.1014
10^8	0.000340	0.000401	0.000406	0.4090	0.8045	1.1130
10^{40}	0.000340	0.000401	0.000405	0.4082	0.8047	1.1153
∞	0.000340	0.000401	0.000405	0.4082	0.8047	1.1153

TABLE 1. Absolute error of volume conservation and percent total energy loss for the plunging free-surface simulation at $t = 1.2$, 1.4 and 1.5 with different smoothing parameter λ values.

h_{max}	Volume error	Energy loss (%)	I_κ	Volume error	Energy loss (%)
0.040	0.000386	3.0828	$2\pi/10$	-0.000265	3.2012
0.035	0.000276	2.4477	$2\pi/15$	-0.000065	2.3279
0.030	0.000254	1.6191	$2\pi/20$	0.000065	1.7173
0.025	0.000133	1.3357	$2\pi/25$	0.000095	1.5451
0.020	0.000049	0.9918	$2\pi/30$	0.000133	1.3357

TABLE 2. Absolute error of volume conservation and percent total energy loss for the plunging free-surface simulation at $t = 1.4$, with different values for the maximal segment size h_{max} and mesh-function increment I_κ

increment I_κ is shown in table 2 for the volume error and energy loss at $t = 1.4$ with $\lambda = 10^{10}$, $h_{min} = 0.001$, and (*a*) $I_\kappa = 2\pi/30$, $h_{max} = 0.04$, 0.035, 0.03, 0.025 and 0.02; and (*b*) $h_{max} = 0.025$, $2\pi/I_\kappa = 10$, 15, 20, 25, 30. Both volume error and energy loss decrease with decreasing h_{max}. The energy loss decreases when I_κ decreases (finer grid), whereas the volume conservation changes sign from a net loss to a net gain. The minimum segment size h_{min}, which controls the highest resolution of discretization, is found to have only a negligible effect on the simulation results.

Next we test the adaptive rediscretization algorithm for the roll-up of a periodic vortex sheet with initially constant strength and a small-amplitude perturbation (Krasny 1986*b*). We plot in figure 2 the vortex roll-up at $t = 2.0$ with $h_{max} = 0.1$, $h_{min} = 0.0025$, $I_\kappa = \pi/10$ and $\lambda = 10^{40}$, 10^{10} and 10^6. The inner spiral of the roll-up is amalgamated into a point vortex, as described in the next section, with a 2π cutoff winding angle. The results show very little difference in the vortex sheet roll-up between the strong smoothing ($\lambda = 10^6$) and the effectively non-smoothing case ($\lambda = 10^{40}$). Also plotted in figure 2 is the result using the vortex-blob method (Krasny 1986*b*) with the blob radius $\delta = 0.12$ and 500 vortex blobs. The comparison between the solutions by the present scheme and the vortex blob method is very close for the outer-spiral turns, demonstrating the accuracy of the present result and also the minimal effect of amalgamation on the global motions.

Figure 3 shows the roll-up at $t = 2.0$ for different mesh-function increments $\pi/I_\kappa = 5$, 10 and 15. The resolution within the rolled-up spiral is improved, as expected, with increasing I_κ. The effect of varying the maximal segment size h_{max} on the vortex sheet roll-up is shown in figure 4. The vortex sheet positions for different values of h_{max} are very close in the rolled-up region except near the braid. The results also demonstrate that the influence of the initial discretization on vortex roll-up since initially all segment sizes are approximately equal to h_{max}. Unlike the free-surface case in which the result converges with decreasing h_{max}, here reducing segment size

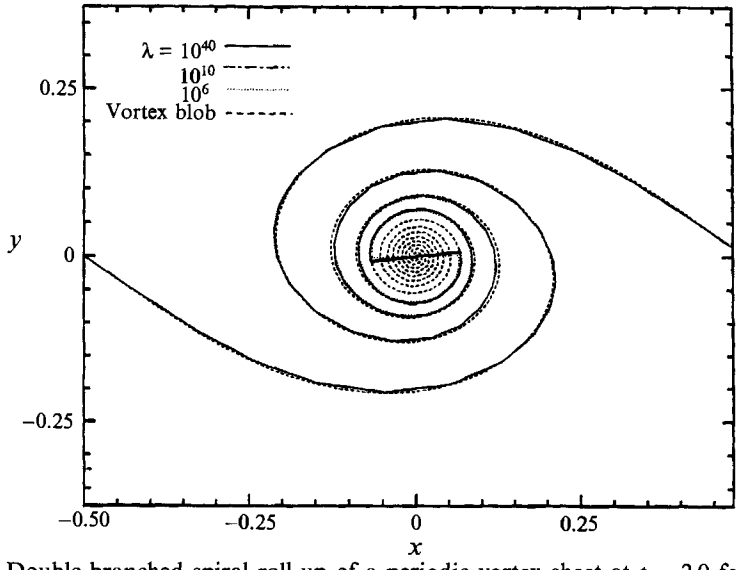

FIGURE 2. Double-branched spiral roll-up of a periodic vortex sheet at $t = 2.0$ for different values of the smoothing parameter $\lambda = 10^6$ 10^{10} and 10^{40}; and by a vortex blob method with 500 vortex blobs and a blob radius $\delta = 0.12$.

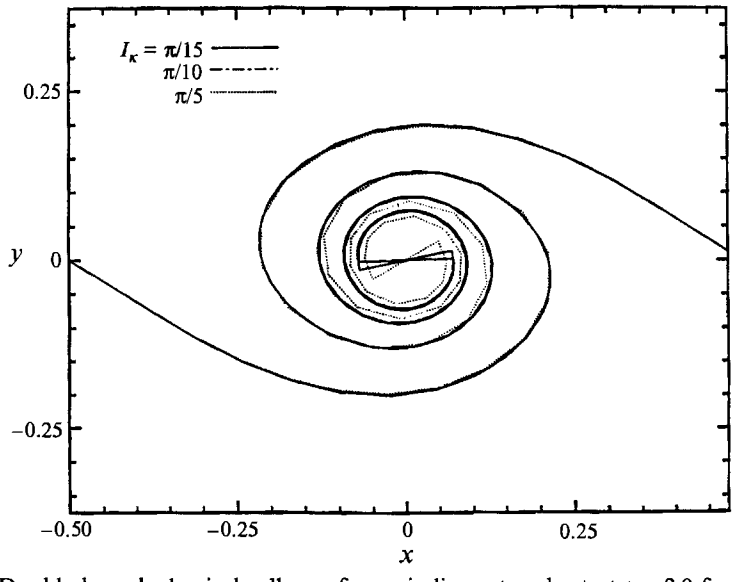

FIGURE 3. Double-branched spiral roll-up of a periodic vortex sheet at $t = 2.0$ for different values of the mesh-function increment $I_\kappa = \pi/15$, $\pi/10$ and $\pi/5$.

introduces modes with higher growing rates. Nevertheless, the global features of the roll-ups are the same with the same embedded initial perturbation.

3.3. *Amalgamation of single- and double-branched spirals*

To avoid numerical difficulties in the simulation of an asymptotically tightened and infinitely wound spiral roll-up, we approximate a single- or double-branched spiral vortex sheet by a single core vortex connected to a finite-winding-number vortex spiral outside (e.g. Pullin & Phillips 1981; Hoeijmakers & Vaatstra 1983). The

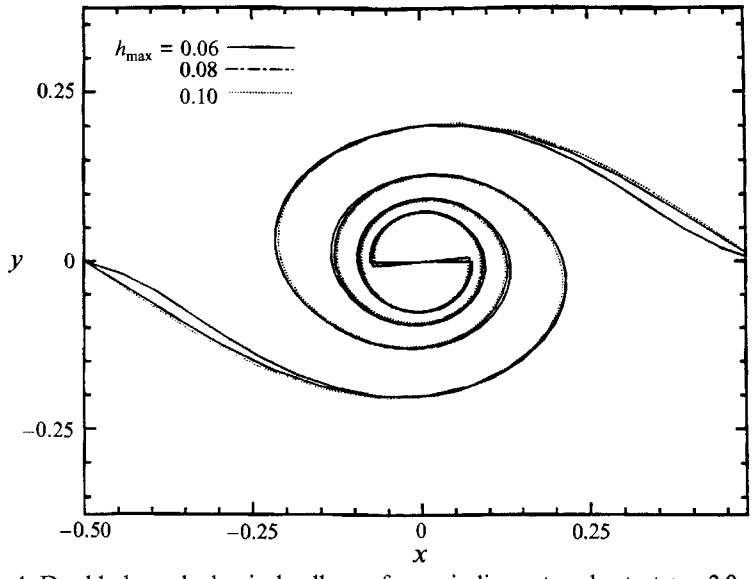

FIGURE 4. Double-branched spiral roll-up of a periodic vortex sheet at $t = 2.0$ with different maximum segment sizes $h_{max} = 0.1$, 0.08 and 0.06.

single-branched spiral roll-up develops from the starting vortex shed at $t = 0$ which continues to roll up into a spiral as time increases. The double-branched roll-up results from steepening of the circulation distribution along the shear layer. In both cases, the excess portion of the shear layer is amalgamated into the core vortex whenever the winding angle of the spiral roll-up exceeds a prescribed value. The amalgamation into a core vortex in effect approximates the steep circulation distribution by a step function. The strength and position of the amalgamated vortex are determined according to the conservation of circulation and linear moment of the circulation.

Figure 5 shows the effect of amalgamation on the evolution of (*a*) a single-branched spiral resulting from the roll-up of a vortex sheet shed by a moving plate with $\pi/2$ angle of attack; and (*b*) a double-branched spiral roll-up of a periodic vortex sheet. By varying the cutoff winding angle, it is seen that the application of amalgamation has a negligible effect on the motions outside the innermost turns of the single- and double-branched spirals.

3.4. *Accuracy of numerical time integration*

As shown in Dommermuth *et al.* (1988), the explicit fourth-order Runge–Kutta time integration for linearized free-surface boundary conditions is conditionally stable and mildly dissipative. The Courant condition for the stability of the Runge–Kutta method is: $\Delta t^2 \leqslant 8Fn^2\Delta s/\pi$, where Δt is the time step of integration and Δs the segment size on the free surface. For our simulations in §4, the typical minimal free-surface segment is 0.01, and the time step is 0.005 which is much less than that required by the (linearized) Courant condition.

To check the accuracy and convergence of the time-stepping procedure for the vortex sheet shedding and tracing, we consider the shedding and subsequent roll-up of the vortex sheet shed by a plate moving perpendicularly in infinite flow. Figure 6 shows the vortex sheet positions at $t = 4.0$ obtained using different integrating time steps ($\Delta t = 0.04$, 0.02, 0.01 and 0.008) of the Runge-Kutta scheme. The monotonic convergence with Δt is clearly demonstrated.

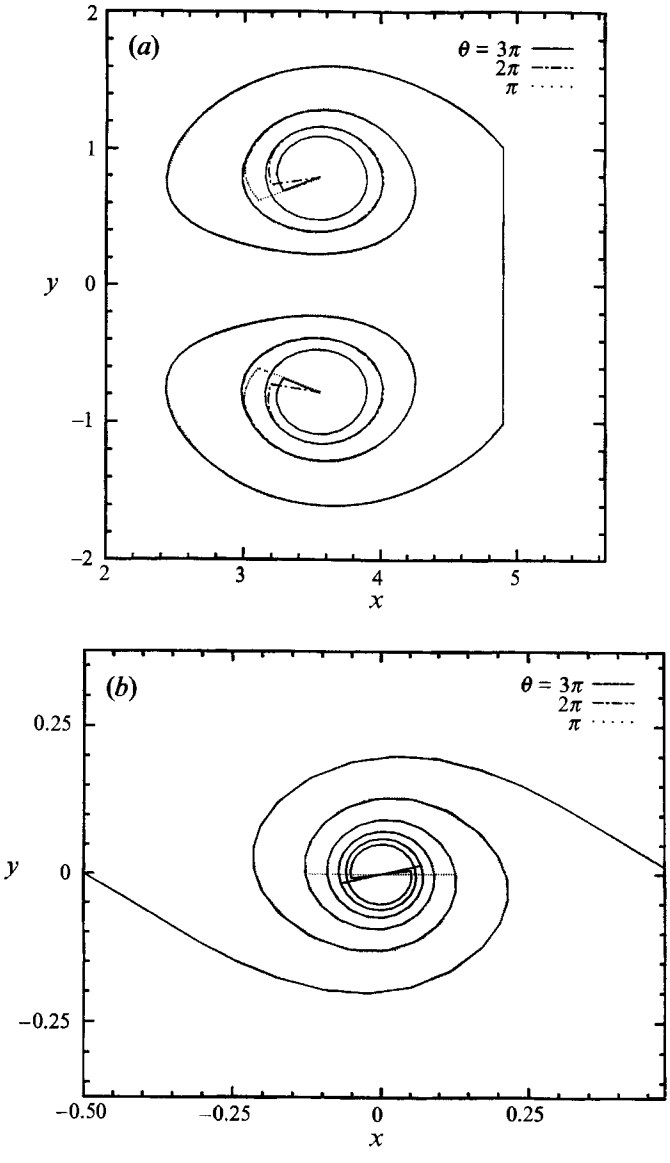

FIGURE 5. Application of amalgamation with cutoff winding angles $\theta = \pi$, 2π and 3π for (*a*) a single-branched spiral roll-up at $t = 5.0$ shed by a moving plate in infinite flow; and (*b*) a double-branched spiral roll-up of a periodic vortex sheet at $t = 2.0$.

3.5. *Effect of grid spacing on the plate*

The discretization of the plate segment affects both the motions of the intersection points and the vortex shedding at the separation point. Careful studies were carried out by Lin (1984) regarding the effect of grid spacing near the intersection point between a moving wall and a free surface. For abrupt starting motions, the free surface at the wall rises sharply forming a long thin upward jet. As the grid density near the intersection corner is increased, the representation of the jet is improved, but the effect on the global free-surface motion is small.

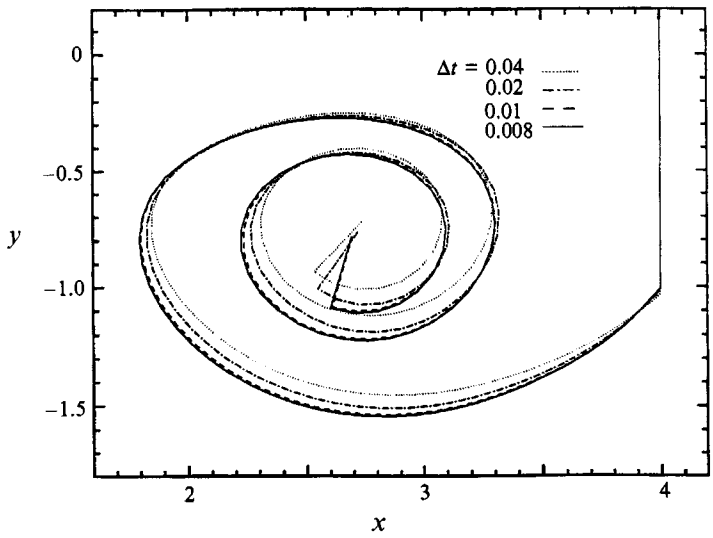

FIGURE 6. Single-branched spiral roll-up at $t = 4.0$ shed by a moving plate in infinite flow with different integrating time steps $\Delta t = 0.04$, 0.02, 0.01 and 0.008.

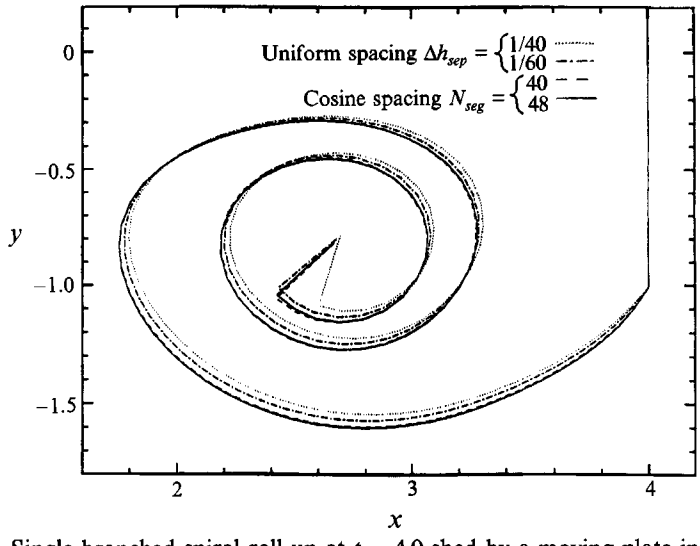

FIGURE 7. Single-branched spiral roll-up at $t = 4.0$ shed by a moving plate in infinite flow with different uniform- and cosine-spaced segments on the plate.

The grid spacing near the separation point is, however, more sensitive since it affects not only the vortex shedding but also the later motions of the vortex sheet. To evaluate these effects, we again consider the perpendicular starting motion of a plate in infinite fluid using both cosine spacing and a two-zoned uniform spacing with different constant segment sizes on the two regions of the plate. Figure 7 shows the resulting shed spiral at $t = 4.0$. The two-zoned uniform spacing is arranged such that finer segments ($h_{sep} = 1/40$ and $1/60$) are distributed within a quarter of the length of the plate from the separation point, and the rest of the plate is discretized with constant segments size $h = 1/28$. Two cosine-spacing grids with total segment number $N_{seg} = 40$ and 48 are also tested. For $N_{seg} = 48$, the segment above the separation

point is only approximately 0.002, which is significantly smaller than that in the two-zoned uniform grids. The profiles are virtually indistinguishable for $N_{seg} = 40$ and 48 cosine-spacing grids. The two-zoned uniform spacing results show smooth convergence to these profiles. For the surface-piercing plate in §4 (with changing submerged length with time), we use two-zoned uniform-spacing along the plate with fixed and finer discretization near the separation point and uniformly rediscretize the rest of plate at each time step.

4. Computational results

4.1. *Critical Froude number for free surface/vortex interactions*

We perform a systematic study of the free surface and shed vortex sheet interactions behind a moving vertical plate by varying the Froude number Fn over the entire range of interest. In addition to the computational parameters discussed in §3, two global conditions may affect the interaction features we obtain: the length of the periodic computational domain and the initial start-up motion of the plate. Extensive tests have been performed (Tsai 1991) to evaluate the effect of changing the length of the periodic computational domain and possible sensitivity to the detailed starting motion of the plate. Selected results are given in Appendix C. Overall, we show that the dependence of the evolutions on Fn as well as the characteristic features of the interaction dynamics are unaffected by our choice of the computational domain length (ℓ=10) or by (small) changes in the initial startup plate motion.

Based on the studies in §3 and Appendix C, for the computational results in the following, we choose the time step of the Runge–Kutta integration $\Delta t = 0.005$ and the periodic domain length $\ell = 10$. The discretization on the plate is uniform with fixed segment size Δh_{sep}=1/60 on the portion within one tenth of the initial submergence from the separation point, and with segment size Δh approximately equal to 0.04 for the rest of the plate which is uniformly rediscretized at every time step. Adaptive rediscretization is applied to the free surface every five time steps with $\lambda = 10^8$, $I_\kappa = \pi/10$, h_{max}=0.06, h_{min}=0.01; it is applied to the vortex sheet every time step with $\lambda = 10^8$, $I_\kappa = \pi/11$, h_{max}=0.06, h_{min}=0.008. In all of our computations, the fluid volume is conserved to at least 10^{-3}, and the total energy (compared to work done) conserved to within 4% for the duration of the simulations. All our simulations are typically continued to a point limited by the applicability of the present numerical method — namely, when a plunging free surface re-enters the fluid, or when a vortex sheet and the free surface or branches of a vortex spiral cross each other. The computer run time for a typical simulation, for example the one for figure 11, is about two hours on a Cray Y-MP supercomputer.

From our numerical simulations, three qualitatively different classes of interactions can be identified, corresponding to subcritical ($Fn \lesssim 0.7$), transcritical ($Fn \sim 0.7$–1.0), and supercritical ($Fn \gtrsim 1.0$) values of Fn. The salient and characteristic features of these three classes of interaction dynamics within the near wake of the plate can be summarized as follows (see figures 8–15):

Subcritical Fn ($Fn \lesssim 0.7$) Rapid development of the free surface due to forcing of the plate leads to free-surface plunging breaking before significant interactions with the starting single-branched spiral vortex can develop.

Transcritical Fn ($Fn \sim 0.7$–1.0) Backwards propagating free-surface set-down pushes backwards the single-branched spiral and stretches the vortex sheet. The

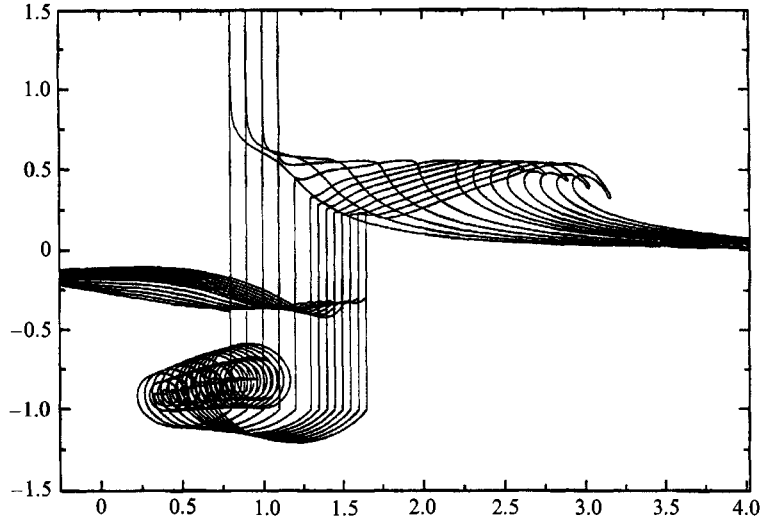

FIGURE 8. Evolution of the free surface and vortex sheet in the wake of a moving vertical plate for a subcritical Froude number $Fn = 0.5$.

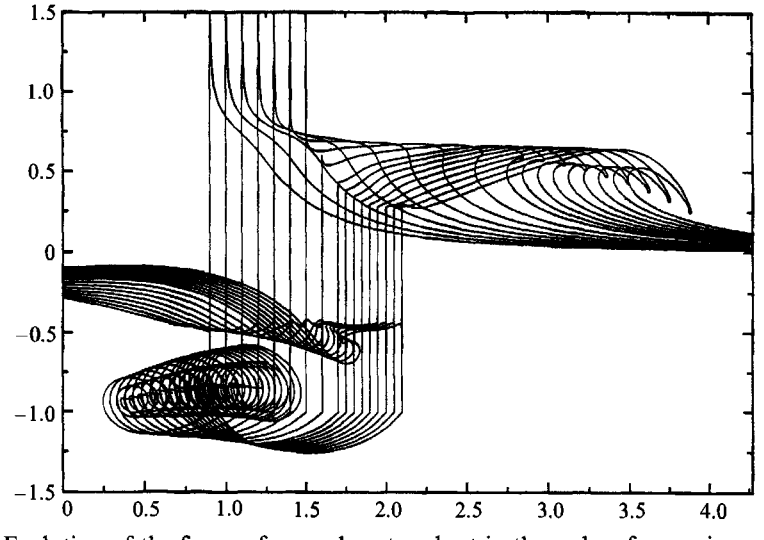

FIGURE 9. Evolution of the free surface and vortex sheet in the wake of a moving vertical plate for a subcritical Froude number $Fn = 0.6$.

stretched vortex sheet rolls up into a series of double-branched spirals with however limited interactions with the free surface.

Supercritical Fn ($Fn \gtrsim 1.0$) In contrast to the transcritical case, the double-branched spirals form near the free surface resulting in significant interactions and prominent free-surface features.

4.1.1. *Subcritical Froude number* ($Fn \lesssim 0.7$)

Figures 8 and 9 show representative evolutions of the subcritical Froude number motions at $Fn = 0.5$ and 0.6. At the early stage, a vortex sheet is shed from the separation point which quickly rolls up into a single-branched spiral. Owing to the impulsive motion of the plate, the free surface on the forward side of the plate shoots up rapidly in the form of a thin jet. Numerical difficulties associated with simulating

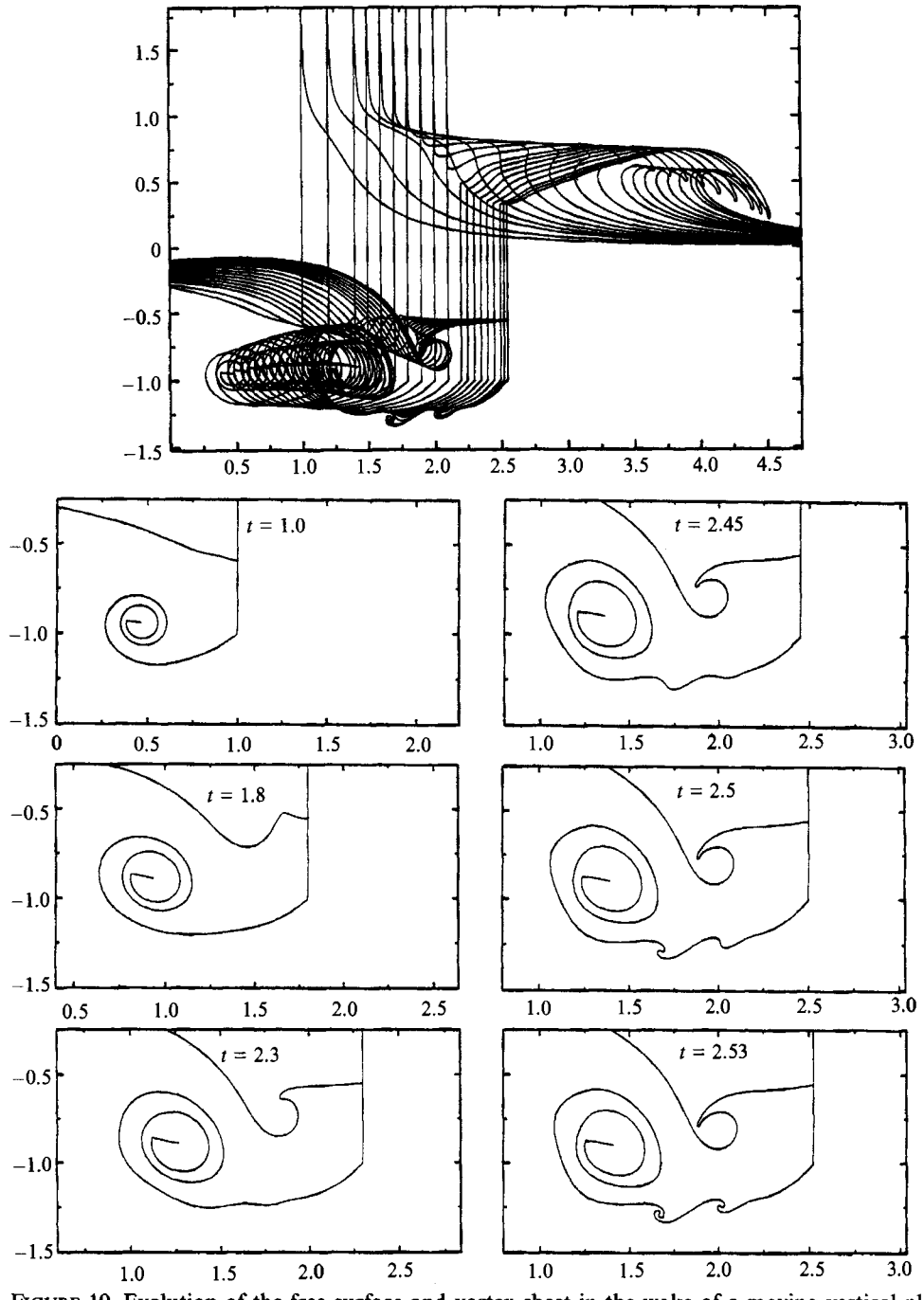

FIGURE 10. Evolution of the free surface and vortex sheet in the wake of a moving vertical plate for a transcritical Froude number $Fn = 0.7$. Details at $t = 1.0$, 1.8, 2.3, 2.45, 2.5 and 2.53.

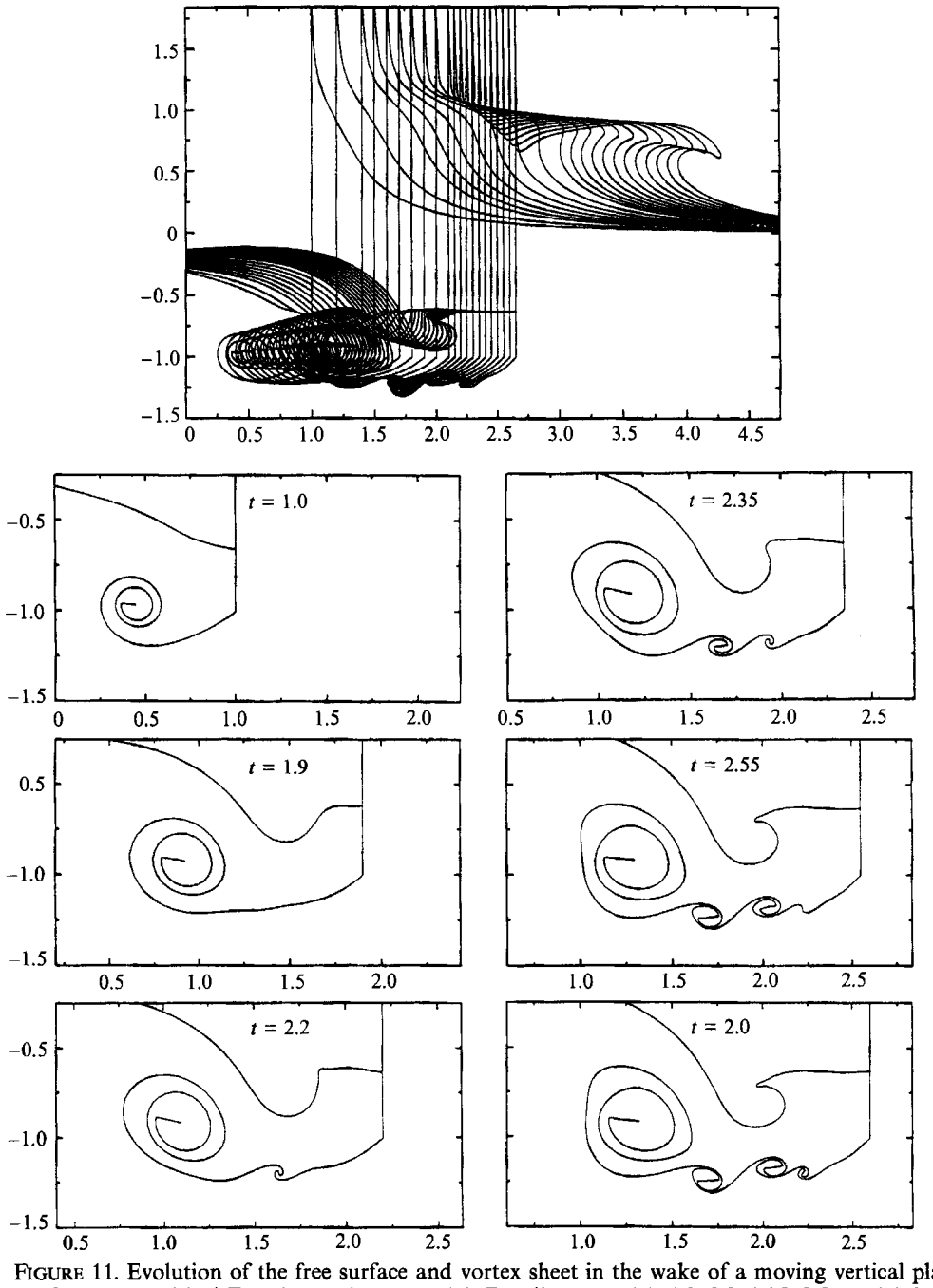

FIGURE 11. Evolution of the free surface and vortex sheet in the wake of a moving vertical plate for a transcritical Froude number $Fn = 0.8$. Details at $t = 1.0$, 1.9, 2.2, 2.35, 2.55 and 2.6.

a very thin film on the forward face are avoided by cutting that portion of the film whose thickness is less than a small fraction (we use 2%) of the local segment length, and a new intersection point is specified. In contrast, the intersection point on the lee side is drawn down and meets the plate at a finite contact angle.

As time proceeds, the single-branched spiral grows in size and the vortex sheet

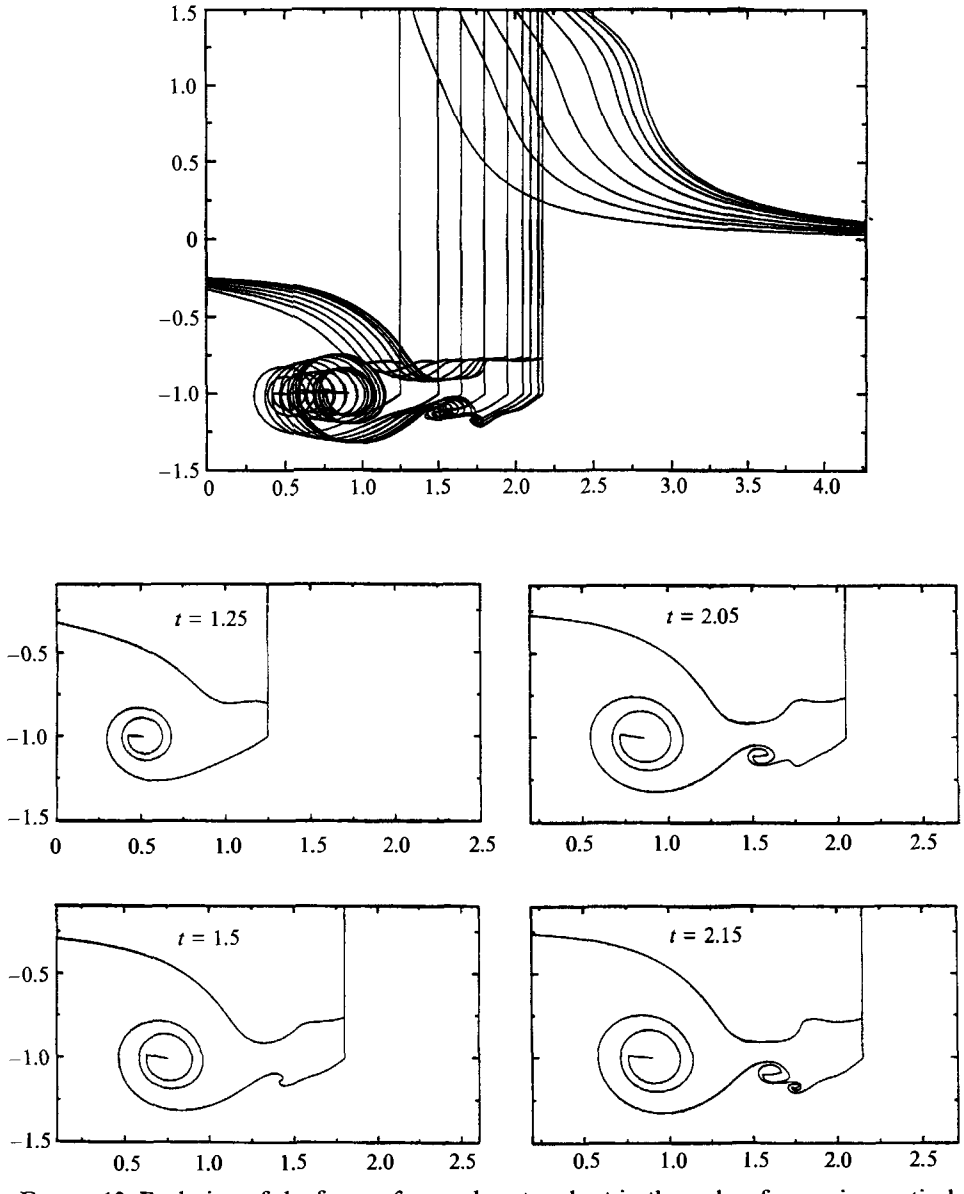

FIGURE 12. Evolution of the free surface and vortex sheet in the wake of a moving vertical plate for a transcritical Froude number $Fn = 1.0$. Details at $t = 1.25$, 1.65, 1.8, 1.95, 2.05 and 2.15.

continuously rolls into the spiral centre. A free-surface disturbance propagates away from the forward face of the plate, eventually forming a plunging breaker. (Our simulations stops shortly before re-entry of the plunger). On the lee side of the plate, a smaller backward propagating wave front is formed near the plate which ultimately also breaks. Consistent with and similar to the infinite-fluid ($Fn = 0$, e.g. figure 5*a*) case, the single-branched spiral remains attached to the plate. The centre of roll-up, however, becomes shallower as it grows, resulting in a small deformation of the free surface. The free-surface and vortex sheet evolutions for this range of Froude numbers are thus characterized by negligible to weak interactions between the two.

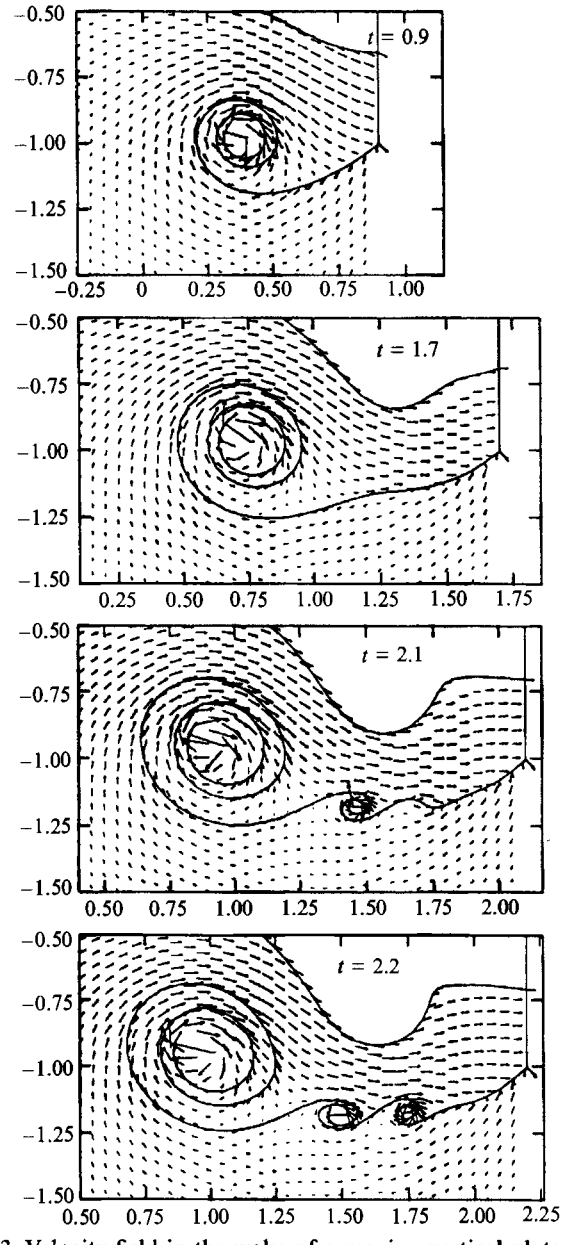

FIGURE 13. Velocity field in the wake of a moving vertical plate for $Fn = 0.9$ at $t = 0.9$, 1.7, 2.1 and 2.2.

4.1.2. *Transcritical Froude number* ($Fn \sim 0.7$–1.0)

The early stages of the free-surface and vortex-sheet evolutions are similar for the three classes. After the single-branched spiral develops, however, significantly different interactions are observed for the transcritical and supercritical Froude number ($Fn \gtrsim 0.7$) cases.

Figures 10–12 show the evolution of the free surface and vortex sheet for $Fn = 0.7$, 0.8 and 1.0 respectively, illustrating the salient features of the transcritical interactions in the wake of the plate. The depression of the free surface on the lee side of the

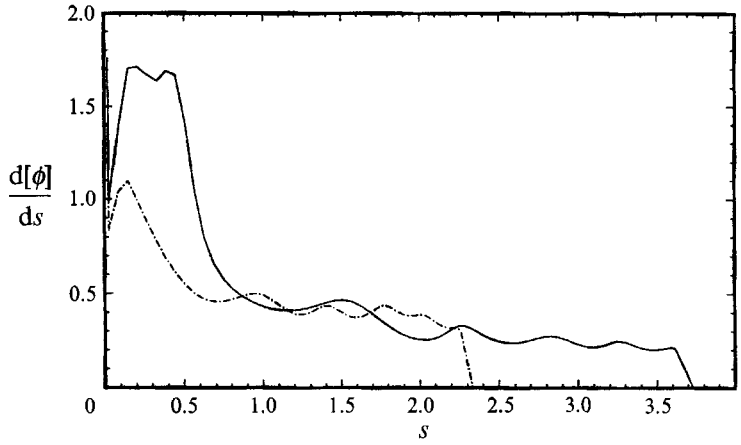

FIGURE 14. Vorticity strength along the vortex sheet as a function of the arclength s measured from the separation point for $Fn = 0.9$ at $t = 0.9$ (dash-dotted line) and 1.7 (solid line).

plate pushes the single-branched vortex spiral downstream causing the vortex sheet to stretch between the single-branched roll-up and the shedding point. At this stage, the rate of vortex shedding at the separation point decreases to a small value (figure 17) and finite-amplitude Kelvin–Helmholtz instabilities develop on the stretched portion of the vortex sheet. As time proceeds, these instabilities grow and eventually roll up into double-branched spirals as shown in figure 10 at $t > 2.45$ for $Fn = 0.7$, figure 11 at $t > 1.9$ for $Fn = 0.8$, and figure 12 at $t > 1.8$ for $Fn = 1.0$.

The onset of Kelvin–Helmholtz instabilities is shown for the $Fn = 0.9$ case in figure 13 which plots the velocity vector fields in the wake of the plate at different times. At the initial stage, $t = 0.9$, the wake flow is mainly influenced by the rolled-up starting vortex which has developed to a considerable size. As the large free-surface depression associated with the plate starting motion propagates backward, it prevents the vortex spiral from rising and pushes it further downstream creating a stretched flat vortex sheet between the separation point and the rolled-up spiral ($t = 1.7$). Owing to flows in opposite directions on the upper and lower sides of the stretched vortex sheet, a strong shear develops which amplifies the initial growth of instabilities on the stretched vortex sheet. These instabilities then quickly roll up into double-branched spirals starting from the portion of shear layer near the single-branched spiral ($t = 2.1$ and 2.2).

Note that the present stretching process, which is due to the interaction between the free surface and the shed vortex sheet, differs from the vortex stretching in Moore & Griffith-Jones (1974) wherein the strength of the vortex sheet is a decreasing function of time as in the roll-up of a vortex spiral. As pointed out by Moore & Griffith-Jones, such a decrease of vorticity strength may actually stablize the Kelvin–Helmholtz instability and suppress the growth of short-wave disturbances. The present vortex stretching between the separation point and the rolled-up spiral such as that in figure 13, however, creates an unstable parallel shear flow across the vortex sheet. The reason for that can be see in figure 14 where we show the vorticity strength $\mathrm{d}[\phi]/\mathrm{d}s$ along the vortex sheet at $t = 0.9$ and 1.7 for the same case, where s is the arclength of the vortex sheet from the separation point. As time proceeds, the length of vortex sheet between the roll-up of the spiral and the separation increases (from approximately 0.3 at $t = 0.7$ to 0.8 at $t = 1.7$) but so also does the vorticity strength. Such amplification

in magnitude of the shear flow destablizes the vortex sheet and causes the onset of Kelvin–Helmholtz instability.

The main difference between the transcritical and supercritical cases is in the strength of the interactions between the free-surface waves and the Kelvin–Helmholtz instabilities on the vortex sheet. For transcritical Froude numbers, the double-branched spirals form well below the free surface. The interactions between the free surface and Kelvin–Helmholtz waves are consequently weak and allow the instabilities on the stretched vortex sheet to roll up continuously, forming a series of double-branched spirals. For higher Froude numbers in the transcritical range, e.g. $Fn = 1.0$ at $t = 2.15$ in figure 12, the double-branched spirals interact with each other and may eventually merge into a single vortex spiral.

The free-surface depression behind the plate continues to develop, the backward-facing surface steepens and eventually develops into a backward-plunging wave. The intersection point on the lee side of the plate moves downward with time, asymptotically reaching a constant depth (see figure 19).

4.1.3. *Supercritical Froude number* ($Fn \gtrsim 1.0$)

The features of the free surface/vortex interactions at a later stage for the supercritical Froude number are distinct from those of the transcritical case, as shown in figures 15 and 16 for $Fn = 1.2$ and 1.5 respectively. As in the transcritical cases, the initial rapid free-surface set-down in the lee of the plate pushes the single-branched spiral downward and forms a stretched, unstable vortex sheet. As the Kelvin–Helmholtz instability grows, a single double-branched spiral forms on the perturbed, stretched vortex sheet beneath the forward side of the free-surface depression. Unlike the transcritical cases, such a solitary double-branched spiral grows in size, approaches and eventually becomes entrained into the free surface. The free-surface deformation is strongly affected by the rising double-branched spiral, developing a sharp depression between the single- and double-branched spirals.

In these supercritical cases, the free-surface disturbance on the front side of the plate does not propagate away. The free-surface jet-like elevation on the plate is pushed forward and continues to rise indefinitely in our computations. On the leeward side, the lower intersection point on the plate likewise continues to moves downward (see figure 19), and the free surface eventually sluices from the lower tip of the plate (when our simulations stop).

4.2. *Time evolution of characteristic properties*

To quantify the above observations, we compare the time evolution of physical properties which characterize the Froude-number dependence of the interactions. Figure 17 shows the rate of vortex (circulation) shedding $-\mathrm{d}[\phi]_{\mathrm{sep}}/\mathrm{d}t$ at the separation point for different Fn. Unlike vortex shedding in infinite flow which increases monotonically at later stages, for finite Froude numbers the shedding rates rise to a maximum and then levels off after a characteristic time. The asymptotic shedding rate decreases monotonically with increasing Fn, although it is difficult to discern a qualitative difference between the Froude-number regimes.

To show the effect of the free surface on the motion of the starting single-branched spiral, we plot, in figure 18, the paths of the spiral centre: $(x_{sc} - t, y_{sc})$ for different Fn. For subcritical Fn, the spiral approaches the free surface as it grows. The backward movement of the vortex is due to the growth of the rolled-up spiral and not the free-surface motion. The elevation of the spiral centre decreases monotonically as Fn increases due to interactions with the depressed free surface. In addition, the starting

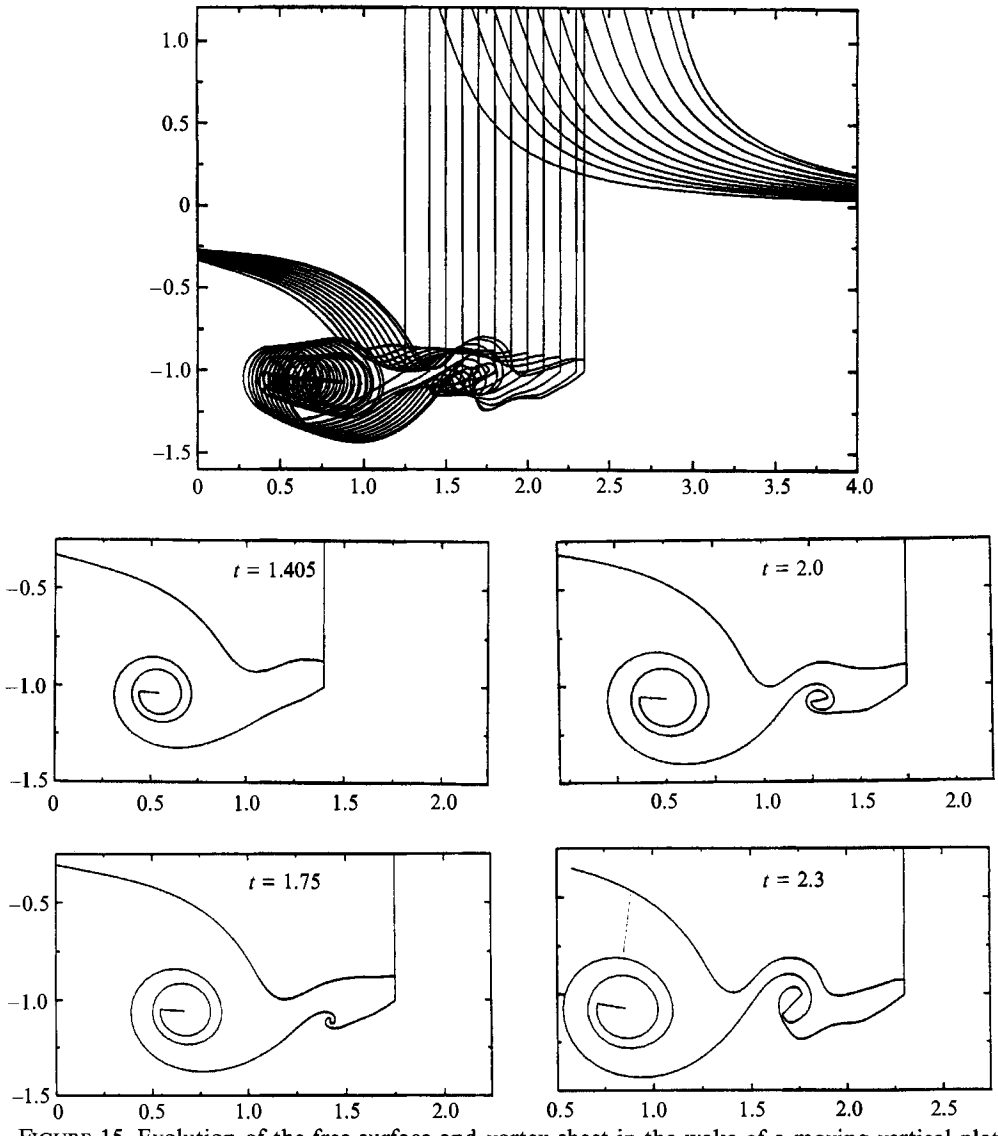

FIGURE 15. Evolution of the free surface and vortex sheet in the wake of a moving vertical plate for a supercritical Froude number $Fn = 1.2$. Details at $t = 1.25$, 1.405, 1.7, 1.75, 2.0 and 2.3.

free-surface depression in the wake pushes the spiral downstream thus stretching the shear layer between the roll-up and the separation point.

The vertical movement of the lower intersection point ($C_f \cap C_p \cap C_s$) is shown in figure 19 where the vertical position $y_{li}(t)$ is plotted. For both subcritical and transcritical Froude numbers ($Fn \lesssim 1.0$), the lower intersection point moves downward first and then oscillates. For supercritical Fn, y_{li} decreases monotonically with time, eventually causing the plate to sluice.

The evolution of the energy (E) of the fluid can be calculated according to (2.10) and is shown in figure 20. Also plotted in the figure is the kinetic energy component due to the vortex sheet (E^v). The total energy increases in time for all Froude numbers since the motion of the plate continues to impart energy to the fluid. The vortical

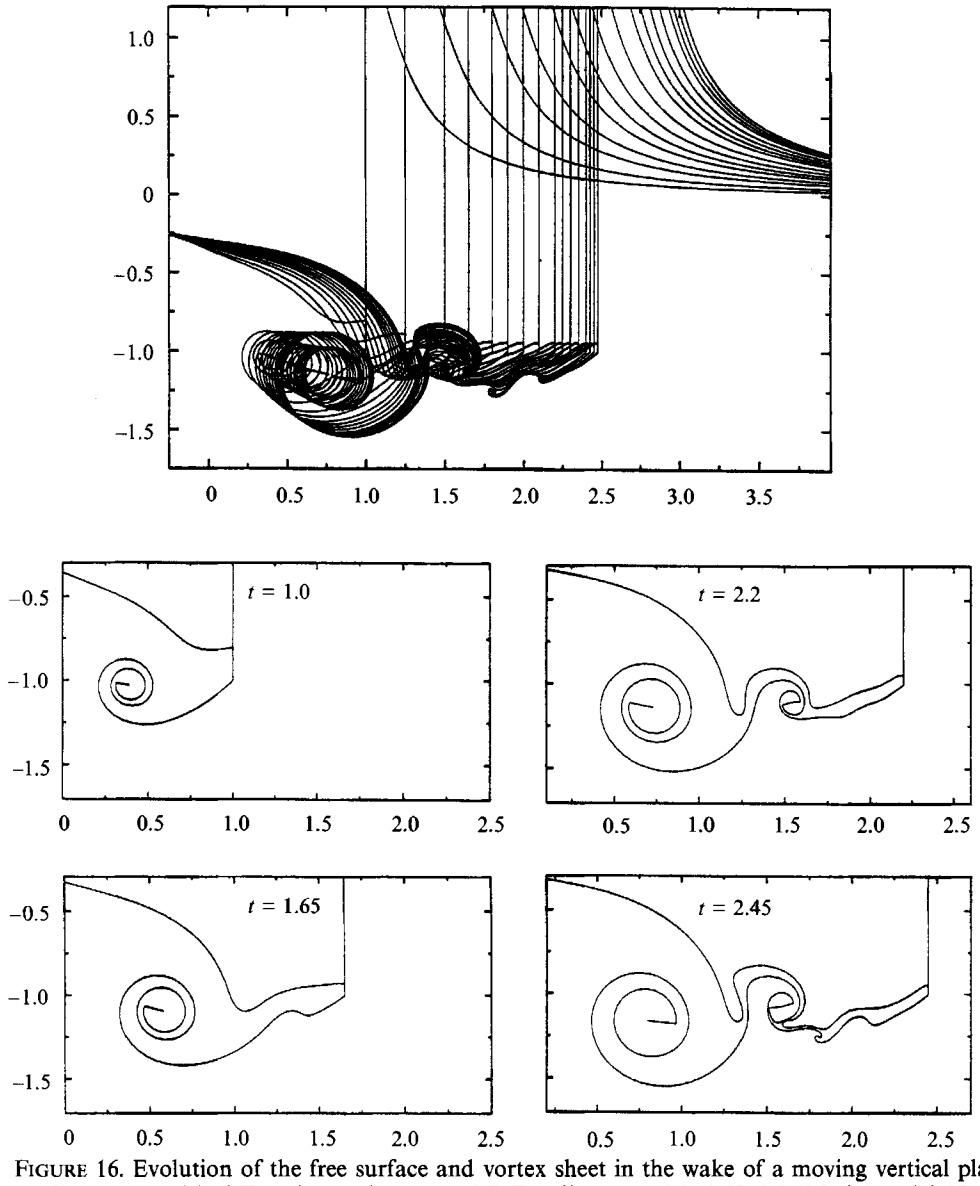

FIGURE 16. Evolution of the free surface and vortex sheet in the wake of a moving vertical plate for a supercritical Froude number $Fn = 1.5$. Details at $t = 1.0$, 1.65, 2.0, 2.2, 2.4 and 2.45.

part of the kinetic energy shows a clear distinction between the subcritical and higher Froude numbers. For subcritical Fn, E^v rises steadily with increasing time consistent with an effectively attached single-branched shed vortex spiral, while for higher Fn, E^v reaches steady asymptotes after $t = O(1)$ as interactions with the free surface cause the starting spiral to be detached.

Finally, we show the time histories of the unsteady horizontal force acting on the plate F_x, and the component of the force due to the vortex sheet F_x^v in figure 21. Note that F_x equals the power input by the plate or equivalently the rate of total energy change in the fluid. For subcritical Fn, the total force first increases with time and then decreases rapidly. During the time when the total force decreases, the component

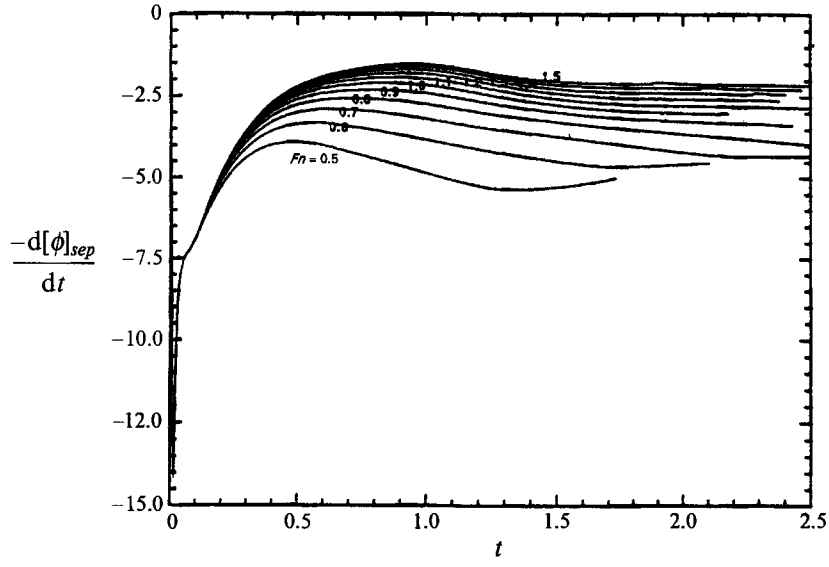

FIGURE 17. Time evolution of the rate of vortex (circulation) shedding $-d[\phi]_{sep}/dt$ from the separation point for different Froude numbers.

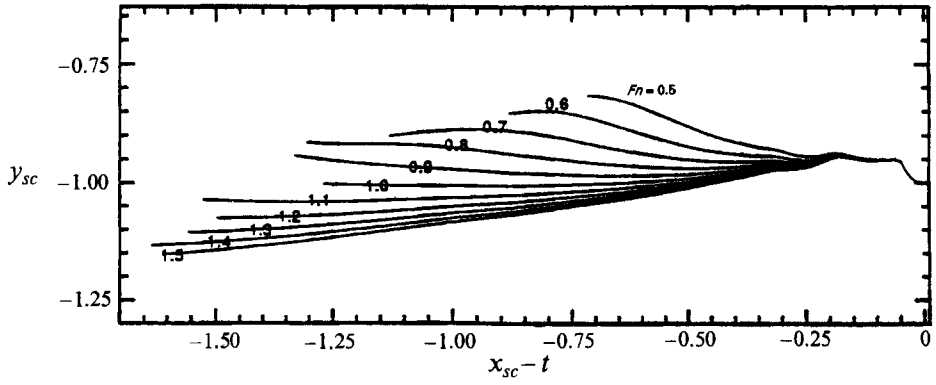

FIGURE 18. Trajectories of the single-branched spiral centre for different Froude numbers.

due to the vortex sheet increases sharply, eventually contributing to almost all of the total force. For the transcritical and supercritical cases, the total force variation is more gradual. At a later stage, the force due to the vortex sheet is small, indicating the detachment of the rolled-up spiral.

5. Conclusions

The complex interactions between a free surface and a shed vortex sheet in the wake of a moving body are examined and quantified by considering the canonical problem of the starting motion of a partially submerged vertical plate. Depending on the Froude number based on the initial plate submergence, three classes of interaction dynamics are identified. For subcritical Froude number ($Fn \lesssim 0.7$), the free surface breaks on both forward and backward faces before significant interactions with the shed vortex sheet occur. In the higher Froude number range ($Fn \gtrsim 1.0$), the strong drawn-down deformation of the free surface on the rearward face stretches

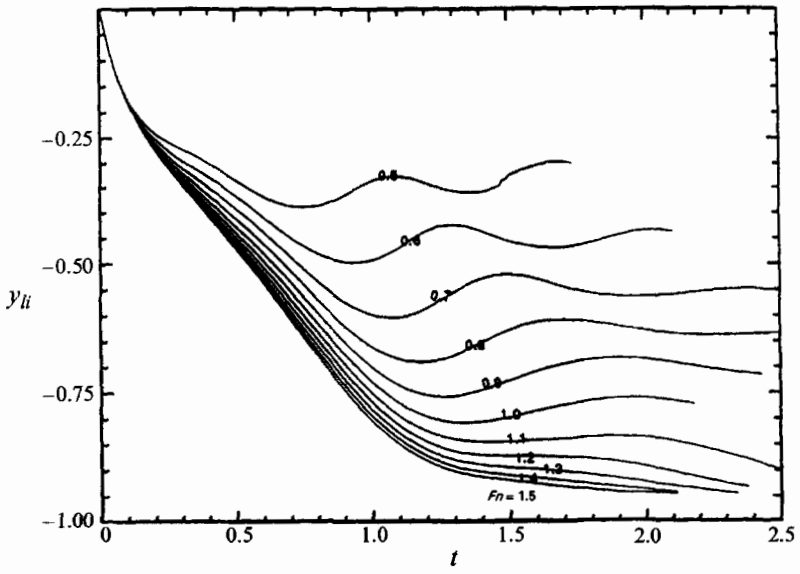

FIGURE 19. Time evolution of the vertical position of the lower intersection point y_{li} for different Froude numbers.

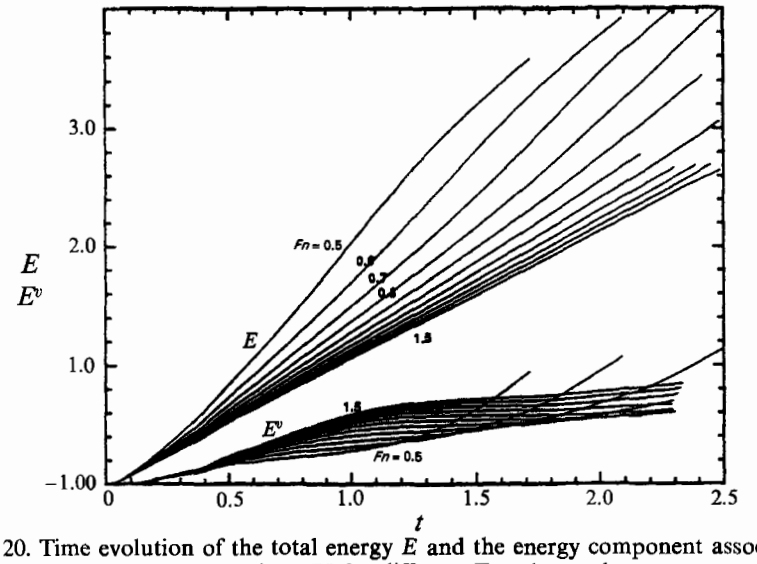

FIGURE 20. Time evolution of the total energy E and the energy component associated with the vortex sheet E^v for different Froude numbers.

the trailing vortex sheet and causes finite-amplitude Kelvin–Helmholtz instabilities. For transcritical Froude numbers ($Fn \sim 0.7$–1.0), these instabilities form sufficiently deep below the free surface and allow them to continuously roll up into double-branched spirals. For supercritical Froude numbers ($Fn \gtrsim 1.0$), the instabilities entrain the free surface resulting in prominent free-surface deformations. Our numerical simulations elucidate the underlying mechanisms and basic features of vortex–free surface dynamics, such as free-surface breaking, vortex entrainment, detachment of the starting vortex, stretching of the shed vortex sheet, and single- and double-branched spiral roll-ups.

A numerical scheme based on the mixed-Eulerian–Lagrangian approach and

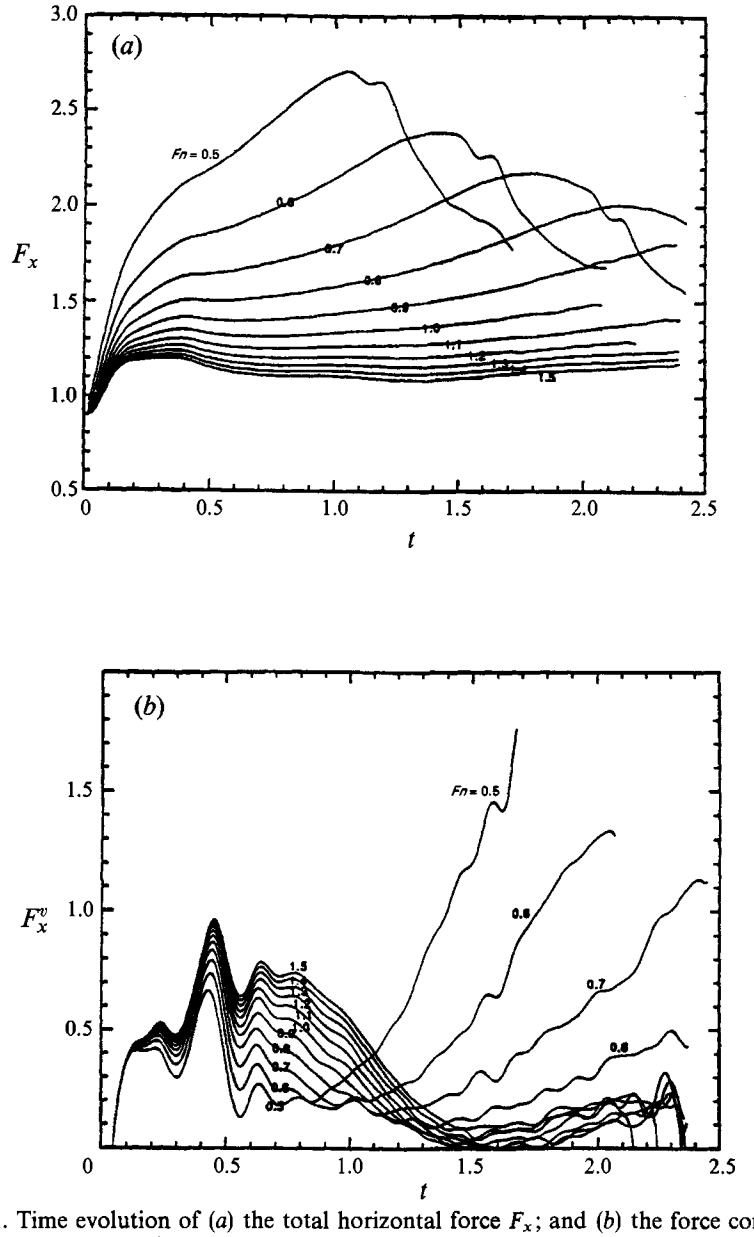

FIGURE 21. Time evolution of (*a*) the total horizontal force F_x; and (*b*) the force component due to the vortex sheet F_x^v; for different Froude numbers.

Cauchy-integral formulation is developed. The scheme is effective and robust and incorporates features such as smoothing spline fitting, mesh-function-controlled rediscretization and spiral amalgamation. Detailed accuracy and convergence tests have been carried out to validate the numerical scheme. Such a numerical scheme can be extended to other vortex–free surface interaction problems such as the damping of floating body due to vortex shedding and the operation of near-surface hydrofoils.

This study is a first step in an effort to understand the intricate features in the wake of a surface-piercing body. Even in the present context of two-dimensional inviscid flows, the resulting interaction dynamics are sublime and complex. Three-

dimensionality and the presence of viscosity lead to new features such as vortex reconnection and breakdown and are the subjects of future research.

This research is financially supported by the Office of Naval Research (Code 11). Most of the computations were performed on the Cray Y-MP at the Pittsburgh Supercomputer Center and on the Cray-2S at Cray Research, Inc.

Appendix A. Discretization and solution of the integral equations

The integral equations (2.1) and (2.2) are discretized by approximating the contour boundaries by piecewise-linear segments, and β and $[\phi]$ by piecewise-linear distributions along the segments. Evaluating at suitable collocation points, the discretized integral equations then take the form of a system of linear equations:

$$\text{Im or Re}\Big[\sum_{z_j\in C_f\cup C_p}\beta_j\Gamma_{jk}+\sum_{z_j\in C_s\cup C_v}[\phi]_j\Gamma_{jk}-2\pi\tilde{\beta}_\infty\Big]=0, \tag{A 1}$$

when $z_k\in C_f$ (imaginary part equations), $z_k\in C_p$ (real part equations), and

$$\text{Im}\Big[\sum_{z_j\in C_f\cup C_p}\beta_j\Gamma_{jk}+\sum_{z_j\in C_s\cup C_v}[\phi]_j\Gamma_{jk}-2\pi\tilde{\beta}_\infty\Big]=-2\pi\psi_k, \tag{A 2}$$

when $z_k\in C_s$. The influence function Γ_{jk} is

$$\Gamma_{jk}=\int_{z_{j-1}}^{z_{j+1}}T_j(z)K(z_j;z_k)\mathrm{d}z, \tag{A 3}$$

and the tent function $T_j(z)$ is defined as

$$T_j(z)=\begin{cases}(z-z_{j-1})/(z_j-z_{j-1}), & z_{j-1}\leqslant z<z_j\\ (z-z_{j+1})/(z_j-z_{j+1}), & z_j\leqslant z<z_{j+1}.\end{cases} \tag{A 4}$$

The integration in the influence function $\Gamma_{k,j}$ which cannot be carried out explicitly is evaluated by subtracting a simple pole $1/(z-z_k+\delta_{jk}\ell)$ from the kernel $K(z_j;z_k)$ as

$$\Gamma_{jk}=\int_{z_{j-1}}^{z_{j+1}}\frac{T_j(z)}{z-z_k+\delta_{jk}\ell}\mathrm{d}z+\int_{z_{j-1}}^{z_{j+1}}T_j(z)\Big[\frac{\pi}{\ell}\cot\frac{\pi}{\ell}(z-z_k)-\frac{1}{z-z_k+\delta_{jk}\ell}\Big]\mathrm{d}z, \tag{A 5}$$

where $\delta_{jk}=1$ when $\text{Re}(z_j-z_k)<-\ell/2$, $\delta_{jk}=-1$ when $\text{Re}(z_j-z_k)>\ell/2$, and $\delta_{jk}=0$ otherwise. The first integral can be evaluated analytically as in Vinje & Brevig (1981). Representing the kernel of the second integral by a multipole expansion up to second order and evaluating the integration gives

$$\begin{aligned}\Gamma_{jk}\approx{}&\frac{z_k-z_{j-1}-\delta_{jk}\ell}{z_j-z_{j-1}}\ln\frac{z_j-z_k+\delta_{jk}\ell}{z_{j-1}-z_k+\delta_{jk}\ell}+\frac{z_k-z_{j+1}-\delta_{jk}\ell}{z_j-z_{j+1}}\ln\frac{z_j-z_k+\delta_{jk}\ell}{z_{j+1}-z_k+\delta_{jk}\ell}\\&+\tfrac{1}{2}(z_{j+1}-z_{j-1})\Big[\frac{\pi}{\ell}\cot\frac{\pi}{\ell}(z_j-z_k)-\frac{1}{z_j-z_k+\delta_{jk}}\\&+\tfrac{1}{3}(2z_j-z_{j-1}-z_{j+1})\Big((\frac{\pi}{\ell})^2\text{cosec}^2\frac{\pi}{\ell}(z_j-z_k)-\frac{1}{(z_j-z_k-\delta_{jk}\ell)^2}\Big)\Big].\end{aligned} \tag{A 6}$$

Appendix B. Adaptive rediscretization algorithm

Given a set of N nodes on the contour boundary $f_j=\{(x_j,y_j)\mid 1\leqslant j\leqslant N\}$, a fitting smoothing spline $S=\{x(s),y(s)\mid s_a\leqslant s\leqslant s_b\}$ is solved by minimizing the

functional

$$K_\lambda(S) = \int_{s_a}^{s_b} [S^{(2)}(s)]^2 \mathrm{d}s + \lambda \sum_{j=1}^{N} [S(s_j) - f_j]^2, \tag{B 1}$$

with natural boundary conditions at $s = s_a$ and s_b (see de Boor 1978 or Lancaster & Šalkauskas 1990 for details). The weighting parameter λ measures the compromise between the smoothness or fitting (decreasing λ) and accuracy or interpolating (increasing λ) of the spline functions.

After the smoothing spline is calculated, the contour is rediscretized based on equidistribution of a 'mesh function' $\kappa(s)$ (Hyman & Naughton 1985) along the contour such that the new node discretization satisfies a prescribed value of

$$I_\kappa = \int_{s_j}^{s_{j+1}} \kappa(s) \mathrm{d}s, \tag{B 2}$$

over each segment j. In the present work, we choose as mesh function the local curvature of the contour. To guarantee a minimal *a priori* accuracy and to prevent the size of segments from decreasing too rapidly, we impose the constraint $h_{\min} \leqslant h_j \leqslant h_{\max}$, where $h_{\max}$ and $h_{\min}$ are prescribed upper and lower limits for the segment sizes. The choice of $h_{\min}$ also guarantees the suppression of instabilities with wavelengths shorter than $2h_{\min}$. In summary, the controlling parameters for adjusting the rediscretization are the weighting parameter for the smoothing cubic spline fitting λ, the integral of the mesh function over each segment I_κ, and the maximal and minimal limits of segment size $h_{\max}$ and $h_{\min}$.

Appendix C. Effects of periodic boundaries and implusive plate motion

Periodic conditions, imposed on the up- and downstream boundaries, are used to confine the computational domain. Although such boundaries eventually interfere with the free surface and vortex sheet motions, our present interest is the interactions in the near wake of the plate. For a given simulation time, we check the effect of the finite boundaries by increasing the length of the computational domain ℓ. Figure 22 compares the results for $\ell = 10$ and 20 for $Fn = 0.8$ and 1.5 at late stages of the simulation. It is evident that the free-surface and vortex evolutions are unaffected by our choice of $\ell = 10$ up to our simulation time of interest.

To keep the dependence of the interaction dynamics to a single parameter — the Froude number, we use an impulsive acceleration of the plate with the plate velocity $U(t)$ given by a Heaviside step function. Since this idealized start-up profile is physically unrealistic, the question remains of whether the classification according to Fn and the characteristic features of the interaction dynamics described in §4 are sensitive to the details of the initial motion of the plate. To investigate this, we consider the case of a smooth startup velocity profile given by $U(t) = \tanh(t/\delta t)$, where δt measures the (finite) startup duration from rest to steady motion.

Our computational experiments with small $\delta t = 0.1$ (approximately 5% of the typical duration of our simulations) show that the main effect of a gradual starting motion is a small delay in the formation and growth of the starting single-branched spiral, effectively shifting the time coordinate (the delay according to the equivalent plate position is given by $(\ln 0.5)\delta t \approx 0.7\delta t$). For subcritical Froude numbers, the single-branched spiral vortex forms well below the surface while the free surface

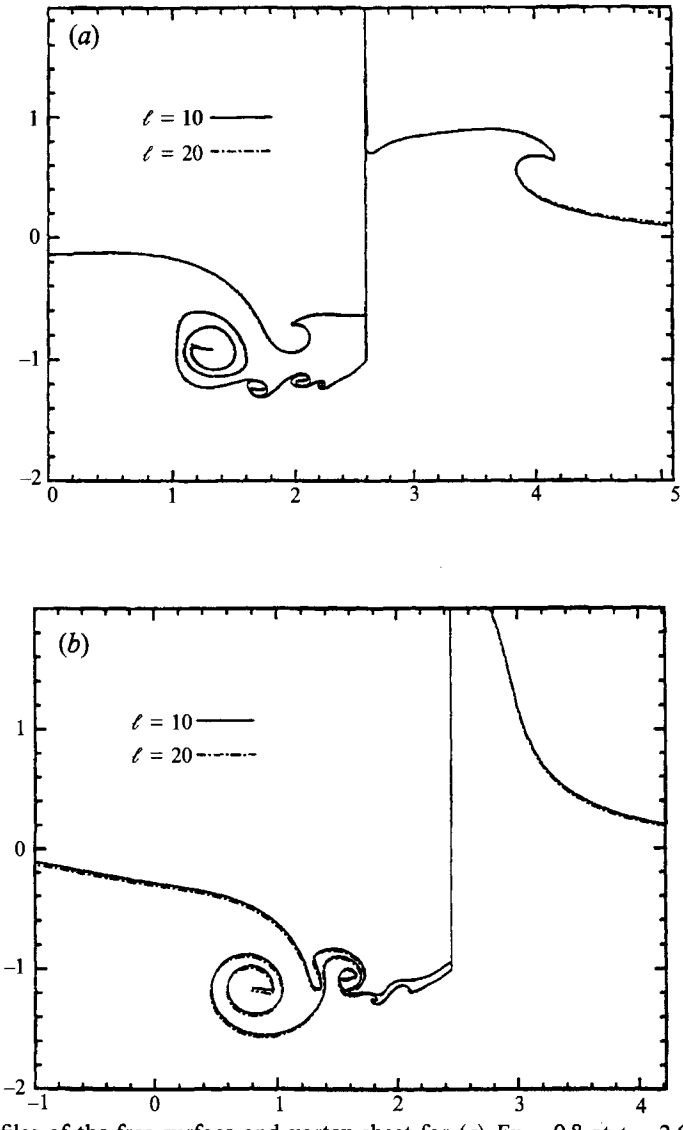

FIGURE 22. Profiles of the free surface and vortex sheet for (*a*) $Fn = 0.8$ at $t = 2.6$ and (*b*) $Fn = 1.5$ at $t = 2.45$; for two lengths of the periodic computational domain $\ell = 10$ and 20.

breaks without significant interactions with the vortex. The dynamical features of the subcritical regime are therefore not affected by details of the initial plate motion.

The effect of the starting motion on the interaction dynamics for transcritical Froude number is shown in figure 23 for $Fn = 0.8$. The plate positions at $t = 1.075$, 1.975, 2.275, 2.425, 2.625 and 2.675 in figure 23 correspond approximately to those at the six time instants given in figure 11 for the impulsively started plate. The delay in the formation and growth of the single-branched spiral is seen by comparing figures 11 and 23. As a result, the stretching of the vortex sheet, the onset of the Kelvin–Helmholtz instabilities, and the formation of the double-branched spirals are likewise postponed. The salient features and development, however, remain unchanged.

Figure 24 shows the corresponding smooth startup evolution for a supercritical

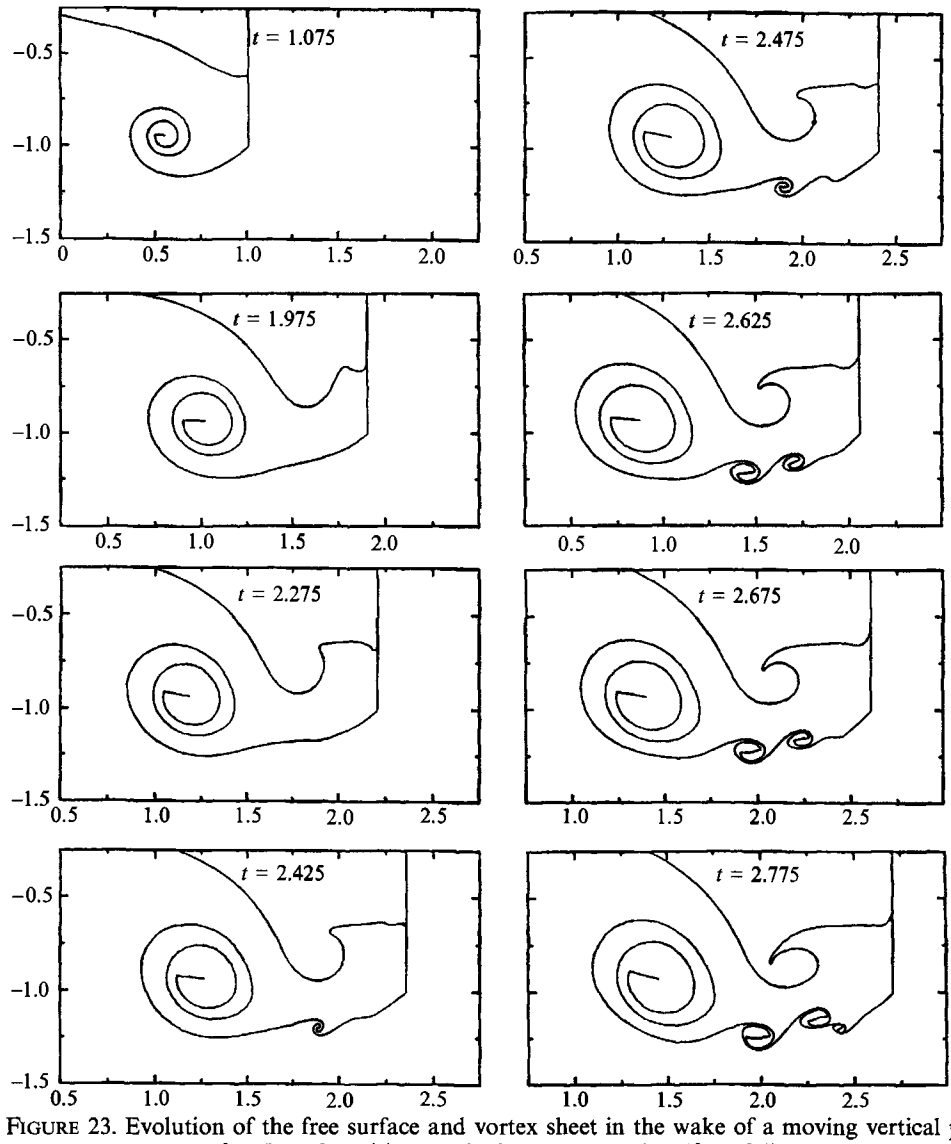

FIGURE 23. Evolution of the free surface and vortex sheet in the wake of a moving vertical plate for $Fn = 0.8$ with a gradual start-up motion ($\delta t = 0.1$).

Froude number ($Fn = 1.5$). The plate positions at the t values in figure 24 are close to those in figure 16. Unlike the sub- and transcritical cases, the delayed formation and growth of the single-branched spiral now have a more noticeable effect on the subsequent interaction dynamics. As before, the delayed single-branched spiral growth postpones the stretching of the vortex sheet as well as the propagation of the free-surface depression. This delay of the set-down propagation accelerates the downward motion of the depressed free surface and consequently the approach of the stretched vortex sheet to the free surface (compare $t = 1.725$ in figure 24 and $t = 1.65$ in figure 16). This expedites the onset of the Kelvin–Helmholtz instability on the stretched vortex sheet and the roll-up of the double-branched spiral (compare $t = 2.075$ in figure 24 and $t = 2.0$ in figure 16). The entrainment of the double-branched spiral into the free surface is also accentuated resulting in steep free-surface disturbances.

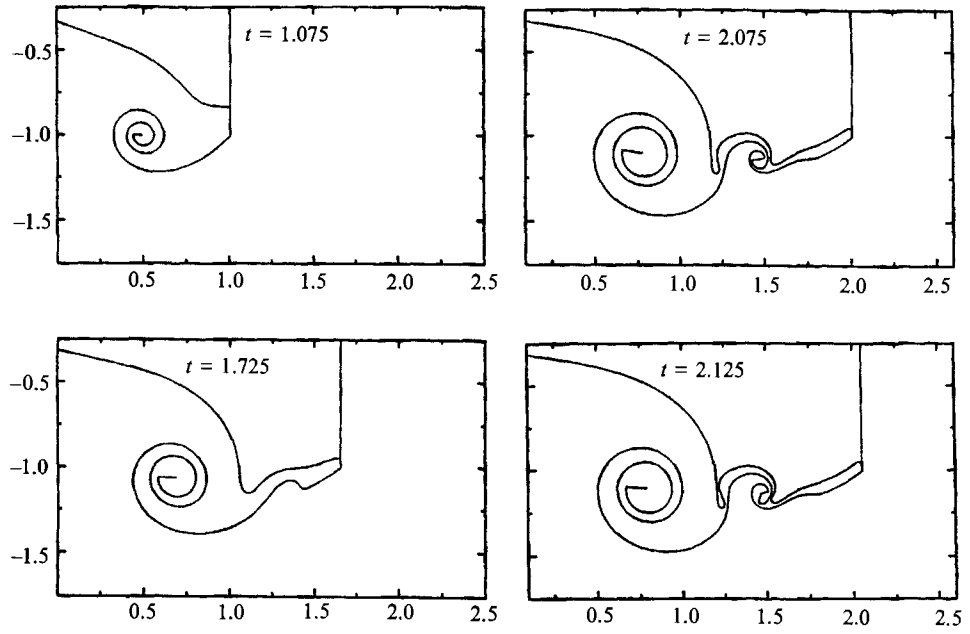

FIGURE 24. Evolution of the free surface and vortex sheet in the wake of a moving vertical plate for $Fn = 1.5$ with a gradual start-up motion ($\delta t = 0.1$).

Eventually, these speed up the collapse of the free surface as shown at $t = 2.125$ in figure 24. Thus a smoother start-up motion in effect *accelerates* the vortex–free surface interactions in the supercritical case. The mechanisms and features, however, remain quite similar.

REFERENCES

BIRKHOFF, G. & FISHER, J. 1959 Do vortex sheets roll up? *Rend. Circ. Mat. Palermo.* **8**, 77–90.

BOOR, C. DE 1978 *A Practical Guide to Splines.* Springer.

CHORIN, A. & BERNARD, P. S. 1973 Discretization of a vortex sheet, with an example of roll-up. *J. Comput. Phys.* **12**, 423.

DIMAS, A. A. 1991 Nonlinear interaction of shear flows with a free surface. PhD thesis, Massachusetts Institute of Technology.

DOLD, J. W. 1992 An efficient surface-integral algorithm applied to unsteady gravity waves. *J. Comput. Phys.* **103**, 90–115.

DOMMERMUTH, D. G., YUE, D. K. P., LIN, W. M., RAPP, R. J., CHAN, E. S. & MELVILLE, W. K. 1988 Deep-water plunging breakers: a comparison between potential theory and experiments. *J. Fluid Mech.* **189**, 423–429.

FALTINSEN, O. M. & PETTERSEN, B. 1982 Vortex shedding around two-dimensional bodies at high Reynolds number. In *Proc. 14th Symp. Naval Hydrodynamics., Ann Arbor, MI*, pp. 1171–1213.

FINK, P. T. & SOH, W. K. 1978 A new approach to roll-up calculations of vortex sheets. *Proc. R. Soc. Lond.* A **362**, 195–209.

GRAHAM, J. H. R. 1983 The lift on an aerofoil in starting flow. *J. Fluid Mech.* **133**, 413–425.

HOEIJMAKERS, H. W. M. & VAATSTRA, W. 1983 A higher order panel method applied to vortex sheet roll-up. *AIAA J.* **21**, 516–523.

HYMAN, J. M. & NAUGHTON, M. J. 1985 Static rezone methods for tensor-product grids. *Lectures in Applied Mathematics*, vol. 22, pp. 321–343. AMS, Providence.

KRASNY, R. 1986*a* A study of singularity formation in a vortex sheet by the point-vortex approximation. *J. Fluid Mech.* **167**, 65–93.

KRASNY, R. 1986*b* Desingularization of periodic vortex sheet roll-up. *J. Comput. Phys.* **65**, 292–313.

LAMB, H. 1932 *Hydrodynamics*. Cambridge University Press.

LANCASTER, P. & ŠALKAUSKAS, K. 1990 *Curve and Surface Fitting*. Academic.

LIN, W. M. 1984 Nonlinear motion of the free surface near a moving body. PhD thesis, Massachusetts Institute of Technology.

LONGUET-HIGGINS M. S. & COKELET, E. D. 1976 The deformation of steep surface waves on water. I. A numerical method of computation. *Proc. R. Soc. Lond.* A **350**, 1–26.

MEIRON, D. I., BAKER, G. R. & ORSZAG, S. A. 1982 Analytic structure of vortex sheet dynamics. Part 1. Kelvin–Helmholtz instability. *J. Fluid Mech.* **114**, 283–298.

MOORE, D. W. 1979 The spontaneous appearance of a singularity in the shape of an evolving vortex sheet. *Proc. R. Soc. Lond.* A **365**, 105–119.

MOORE, D. W. 1981 On the point vortex method. *SIAM J. Sci. Statist. Comput.* **2**, 65–84.

MOORE, D. W. & GRIFFITH-JONES, R. 1974 The stability of an expanding circular vortex sheet. *Mathematika* **21**, 128–133.

NEWMAN, J. N. 1977 *Marine Hydrodynamics*. MIT Press.

PULLIN, D. I. & PHILLIPS, W. R. C. 1981 On a generalization of Kaden's problem. *J. Fluid Mech.* **104**, 45–53.

ROSENHEAD, L. 1931 Formation of vortices from a surface of discontinuity. *Proc. R. Soc. Lond.* A **135**, 170–192.

ROTTMAN, J. W. & STANSBY, P. K. 1993 On the 'δ-equations' for vortex sheet evolution. *J. Fluid Mech.* **247**, 527–549.

SARPKAYA, T. 1989 Computational methods with vortices – The 1988 Freeman scholar lecture. *Trans. ASME* I: *J. Fluids Engng* **111**, 5–52.

SULEM, C., SULEM, P. L., BARDOS, C. & FRISCH, U. 1981 Finite time analyticity for the two and three dimensional Kelvin-Helmholtz instability. *Commun. Math. Phys.* **80**, 485–516.

TSAI, W.-T. 1991 Interactions between a free surface and a shed vortex sheet. PhD thesis, Part 2, Massachusetts Institute of Technology.

TSAI, W.-T. & YUE, D. K. P. 1991 Features of nonlinear interactions between a free surface and a shed vortex shear layer. *Phys. Fluids* A **3** 2485–2488.

VINJE, T. & BREVIG, P. 1981 Nonlinear two-dimensional ship motions. *The Ship Research Institute of Norway, Rep.* R-112.81.

YU, D. & TRYGGVASON, G. 1990 The free-surface signature of unsteady, two dimensional vortex flows. *J. Fluid Mech.* **218**, 547–572.